THE DISCRETE X-RAY SOURCE POPULATION IN M31

G. TRINCHIERI

Osservatorio Astrofisico di Arcetri, Largo E. Fermi 5, 50125 Firenze, Italy; and Harvard-Smithsonian Center for Astrophysics

AND

G. FABBIANO

Harvard-Smithsonian Center for Astrophysics, 60 Garden Street, Cambridge, MA 02138

ABSTRACT

We report the results of the analysis of the entire set of *Einstein* imaging observations of M31. We detect 108 individual X-ray sources, with (0.2–4.0 keV) luminosities ranging from 5×10^{36} ergs s^{-1} to above 10^{38} ergs s^{-1} at the distance of M31 (690 kpc). Fourteen of these sources are luminous enough to perform a spectral fit of the X-ray data. Fourteen sources are found to vary between *Einstein* observations, in addition to the two sources already reported by Collura, Reale, and Peres. We do not find any substantial difference between the luminosity distributions of X-ray sources in the bulge and in the disk, contrary to earlier reports. The luminosity distribution of these X-ray sources is well represented by a power law with slopes between -1 and -0.66 (1 σ). About 20%–30% of the counts detected in the bulge region are not accounted for by the individual sources. This additional emission can be easily explained by the integrated contribution of sources below the detection threshold. Nevertheless, if we use this component to set a conservative upper limit on the emission of a putative gaseous component, we find that no more than $\sim 2 \times 10^{6}$ $M_{\odot}$ of hot gas can be present in the bulge. This limit is consistent with optical, H I, and IR estimates and implies the presence of galactic winds in M31. We present contour maps of the X-ray emission in the central region, and we compare the radial distribution of the surface brightness with the optical profiles. This comparison suggests that the disk is relatively underluminous in X-rays, relative to the stellar content. We compare the spatial distribution of bulge sources with that of optical novae and with emission-line images of the bulge. These comparisons constrain models of formation of low-mass X-ray binaries.

Subject headings: galaxies: individual (M31) — galaxies: interstellar matter — galaxies: X-rays

1. INTRODUCTION

The X-ray emission of normal spiral galaxies has been explained in terms of a collection of bright, individual sources distributed in the disk and bulge region of the galaxies (see Fabbiano 1989 for a review). This interpretation is based on the evidence given by the observations of well-known nearby systems, extrapolated to more distant galaxies, which are thought (with the aid of related evidence) to have similar X-ray properties. It is therefore of fundamental importance to understand the X-ray properties of these nearby examples, for which detailed X-ray maps can be derived, and unambiguous optical or radio identifications of X-ray sources are possible. The Andromeda galaxy is the best subject for an in-depth X-ray study of an early-type spiral system, due to its proximity to us, its large angular dimensions, and its location well outside the obscuring effect of the Galactic disk. Furthermore, an accurate knowledge of the galaxy distance removes a considerable source of uncertainty in the determination of X-ray source luminosities. As summarized in Capaccioli et al. (1989), several methods have been used to determine the distance of M31, which is estimated in the range from ~ 630 to 750 kpc. We have adopted a distance of 690 kpc to derive the intrinsic quantities (see Baade & Swope 1963; it also corresponds to the average value).

The presence of many discrete X-ray sources in M31 is by now well known (Van Speybroeck et al. 1979; Van Speybroeck & Bechtold 1981). Some of these sources were identified with young stellar associations; others, with globular clusters; a few are coincident with supernova remnants (Crampton et al.

1984; Blair, Kirshner, & Chevalier 1981). However, a complete list of source positions and luminosities has never been published. A partial list of positions (not including the very crowded inner bulge region), but not fluxes, was given by Crampton et al. (1984). Moreover, no spectral studies of individual X-ray sources in M31 exist. The only published X-ray spectra are those of the integrated emission of the bulge from *Einstein* data (Fabbiano, Trinchieri, & Van Speybroeck 1987), and of the integrated emission of the galaxy in the harder energy band of *Ginga* (Makishima et al. 1989). Furthermore, short-term variability was studied by Collura, Reale, & Peres (1990), but their study was focused on time variations within single *Einstein* pointings.

The aim of this paper is to complement the previous work on the *Einstein* observations of M31 by presenting a complete study of the X-ray source population. To this end, we have analyzed all the available *Einstein* imaging observations to derive fluxes, spectral characteristics, and long-term variability of the M31 sources.

2. DATA ANALYSIS AND RESULTS

M31 was observed repeatedly with the Imaging Proportional Counter (IPC) and High Resolution Imager (HRI) on board the *Einstein Observatory* (Giacconi et al. 1979). The log of the observations is given in Table 1. Figure 1, adapted from Collura et al. (1990), shows the positions in the sky of the individual IPC and HRI fields. The analysis presented here is based on all of the *Einstein* imaging observations. Each field was analyzed individually, as explained below. Moreover, to

TABLE 1

Log of *Einstein* Observations of M31

Sequence Number	Day	Instrument	Field Center R.A. (1950)	Field Center Decl. (1950)	Exposure Time (s)
573........	1979 Jan	IPC	00^{h}38^{m}00^s	40°24'57"	20434.6
579........	1979 Jan	HRI	00 40 00	40 58 58	28564.0
574........	1979 Jan	IPC	00 40 00	40 58 58	35383.3
575........	1979 Jan	IPC	00 42 36	41 37 58	31668.2
4481........	1979 Aug	HRI	00 37 32	40 30 48	9589.4
4486........	1979 Aug–1980 Jan	HRI	00 39 38	41 14 55	29723.5
4480........	1979 Aug	HRI	00 39 42	40 40 47	26923.5
4479........	1979 Aug	HRI	00 40 00	40 58 58	26024.0
4490........	1979 Aug	IPC	00 40 19	41 03 45	10695.8
4485........	1979 Aug	HRI	00 41 08	41 03 50	24698.9
4484........	1979 Aug	HRI	00 42 49	41 27 51	9959.7
4483........	1979 Aug–1980 Jan	HRI	00 43 16	41 49 04	29088.0
7066........	1980 Jan	HRI	00 40 00	40 58 58	10416.3
5021........	1980 Jul	IPC	00 41 53	40 34 21	7757.5

increase the statistical significance in the central bulge region, we have also merged the three overlapping HRI fields H579, H7066, and H4479 and analyzed the resulting image. However, the two central overlapping IPC fields (I574 and I4490) were analyzed individually to derive source fluxes. Merging the two fields did not reveal the presence of additional sources, and the instrumental support ribs and the field edges complicate the derivation of the source exposure in the merged image. The IPC background subtraction and source fluxes were all estimated using the nominal " broad " energy band of 0.2–3.5 keV (Harnden et al. 1984).

2.1. Background Subtraction

2.1.1. HRI

With the exception of the central region of M31, radial profiles of the HRI fields indicate that the background is relatively flat and constant over the entire field of view. We have therefore used the average field values as the background for sources not in the crowded area of the bulge. This is equivalent to estimating it locally around each source, but with a larger statistical significance. In the bulge region, the background determination is more critical. On the one hand, source crowding prevents us from obtaining a local estimate. On the other hand, the average value obtained from less crowded regions could underestimate the background level, since there could be contributions due to either unresolved, fainter sources or diffuse emission (see § 2.4). Radial profiles of the X-ray surface brightness in four quadrants centered along the major and minor axes (Fig. 2) show several peaks of emissions, corresponding to the many individual sources (see § 2.3), in particular in the inner 200". However, the 350°–80° profile, which is less contaminated by individual bright sources, shows a fairly constant X-ray surface brightness, down to a 100" radius. We
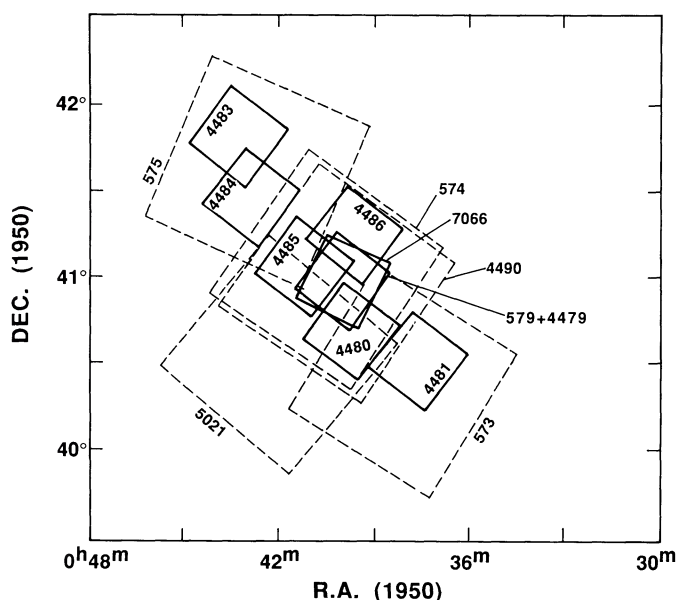
Fig. 1.—The *Einstein* fields pointed at M31. Dashed squares are IPC fields; continuous squares are HRI fields. Sequence numbers are indicated.
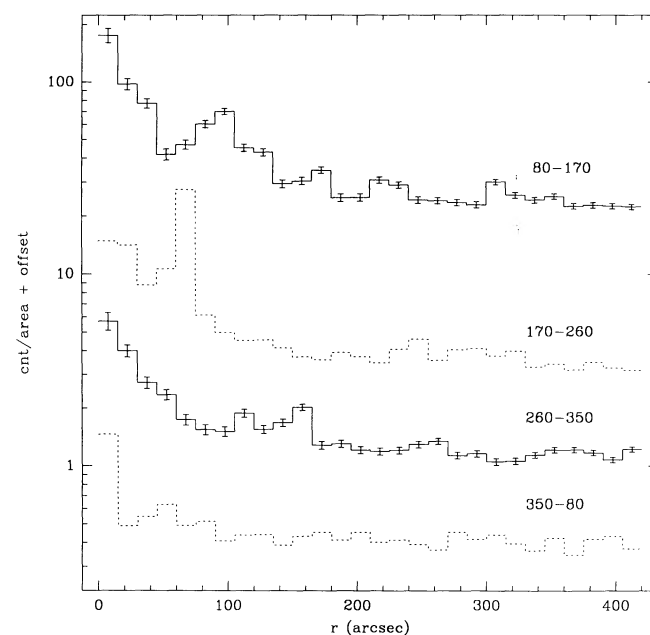
Fig. 2.—Radial distribution of the raw counts (normalized by the area), for the merged HRI field at the M31 center, in four quadrants along the major and minor axes, centered at 0^{h}40^m, 41°0'. The units on the y-axis refer to the 80°–170° profile. To be plotted on the same diagram an offset of 0.6, 1.2, and 1.8 (in the log) has been added to the other profiles.

can therefore approximate the background in the central region by constant values over large areas.

We have adopted the average surface brightness in the 2'–5' region as a background value for all sources within a 5' radius circle. Similarly, an average value was obtained from the annulus from 5' to 9', and for the region outside 9'. For the merged HRI image, the exposure is no longer uniform outside ∼ 10', since the three images used to produce it were obtained at different rotation angles in the sky. For galactocentric distances larger than 9', we used the individual fields to estimate the source count rates, and therefore we have adopted the average field background, as discussed above.

In § 2.4 we will show that there is extended emission not accounted for by the individual sources within a 5' radius contributing ∼ 4300 counts to the total bulge luminosity. The presence of this component raises the local background for each source from our estimates. However, because of the complexity of the image and of the shape of the HRI Point Response Function (PRF), we cannot easily estimate its actual contribution at different radii. If we assume that its radial dependence is similar to that of the optical light (§ 2.2), then the number of counts due to this component within and without 2' should be similar. In this case, our method of background subtraction for sources within the central 2' would have underestimated the background within each 6″7 detection circle by about five counts on average, and our fluxes (§ 2.3) would have to be revised downward. In particular, 11 sources which are now detected above threshold (sources 36, 42, 45, 48, 50, 53, 59, 61, 65, 66, and 72) might become upper limits with a more local determination of the background. A more accurate derivation of source fluxes in the centermost region will have to await the analysis of the *ROSAT* HRI image, which has a sharper PRF than the *Einstein* one.

2.1.2. *IPC*

The IPC fields have the added complication of a radially nonuniform background. Templates that contain the information on the shape and structure of the IPC background are produced by the standard processing system and are normalized to the total number of the nonsource counts in the images (Harnden et al. 1984). In the presence of a low surface brightness extended component, the normalization could however be overestimated. If these low surface brightness features are significantly less extended than the entire IPC field, one can renormalize the background template by comparing the radial profiles of the images and background fields and adjusting the normalization to make the two distibutions match in level where the shape indicates no significant source emission (see Trinchieri, Fabbiano, & Canizares 1987). If, however, there are emission features extending over a large fraction of the field, this method may underestimate them. Since M31 extends over three IPC fields, this may be a reason of concern, resulting in underestimating the surface brightness of the galaxy disk. However, this background subtraction will not affect the estimate of the individual source fluxes, which is the prime aim of this paper. Figure 3 shows the radial profiles of the raw data compared to the background profiles, after these have been renormalized to the data, and the resulting background-subtracted profiles.

2.2. *Contour Maps and Surface Brightness Profiles of the Central Region of M31*

Figure 4a shows an isointensity contour plot of the bulge of M31 obtained with the HRI data at a resolution of 1″ pixel⁻¹.

We have used the merged image, and we have smoothed the data with a Gaussian function with $\sigma = 4''$. A flat-field background has been subtracted. It is evident that the dominant component is represented by ∼ 50 individual sources. A small unresolved component is also present, more visible with smoothings at lower resolution (see § 3). The morphological details of the bulge emission are lost in the IPC data, where this region appears as an extended source slightly elongated in the east-west direction (Fig. 4b). Outside of the bulge, only isolated sources are seen.

A radial surface brightness profile of the emission from the bulge is plotted in Figure 5. The data are binned in concentric circular annuli. Both HRI (from the merged image) and IPC data are included, and normalized in the region outside $r = 3'$ where the Point Response Function of the IPC no longer dominates the profile's shape (cf. Harnden et al. 1984; Mauche & Gorenstein 1986). A comparison with the optical profile, also binned in circular concentric annuli (S. Kent, private communication) is shown as well.

The X-ray data are clearly less smooth than the optical profile, because of the many bright sources individually detected. The composite HRI–IPC profile appears steeper than the optical profile. However, comparison between the HRI profile and the optical profile suggests similar distributions for the X-ray emission and the stellar light in the bulge. The lack of a significant disk component in M31, outside of the individual bright sources, could account in part for the steeper X-ray gradient at larger radii.

2.3. *Individual Source Detections*

The high-resolution HRI fields show ∼ 50 sources in the central region of M31 (Fig. 4a). A similar number of sources is detected at larger galactic radii with both HRI and IPC. Table 2A lists all X-ray sources detected in the M31 fields and their detection parameters. Their spatial distribution is shown in Figure 6. We have used the merged HRI field to derive source counts in the bulge region. IPC counts for individual resolved sources in the central region, which is covered by two IPC fields (cf. Table 1 and Fig. 1) are derived from only one of the two observations (see above). Whenever possible, we used I574 (the longer observation).

Table 2A lists 108 sources detected above a 3 σ threshold in the standard detection cell (equivalent circles of $r = 6''7$ and 90″ for HRI and IPC, respectively). Table 2B lists eight additional sources, which were included in the list of Crampton et al. (1984), but fall below our detection criterion. Column (1) gives our detected source number; Column (2) lists the source number of Crampton et al. (1984) for reference; columns (3) and (4) give the X-ray centroid position. Most of these positions are from the HRI detections. For a few sources common to both IPC and HRI, we have used the more accurate HRI position and we have listed the HRI detected counts and fluxes, for inhomogeneity with most other fluxes. The instrument is given in column (5) (H for HRI, I for IPC). The background-subtracted source counts and statistical errors are given in columns (6) and (7). HRI net counts were derived from detection cell circles in the inner bulge region (resulting in the detection of ∼ 60% of the total source counts). Outside the inner crowded area, source counts in the HRI are derived in the typical 18″ radius circle for point sources, which contains ∼ 76% of the source photons, except in cases of overlapping cells. IPC net counts are from the standard "broad" band (0.2–3.5 keV). IPC source counts are derived in general in the 3' radius standard circle for point sources (containing ∼ 90% of
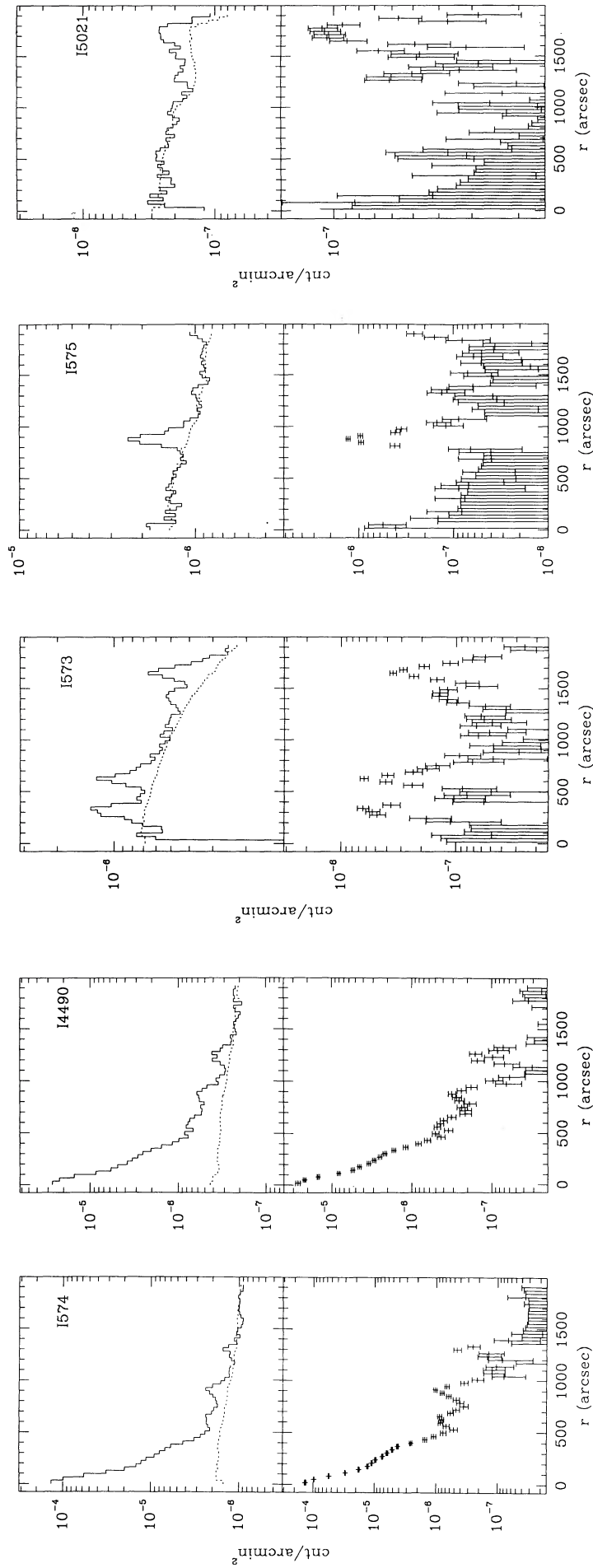
Fig. 3.—*Top*: Radial surface brightness profiles for the IPC raw data (broad-band). The adopted background level is also shown. *Bottom*: The background-subtracted radial profile.
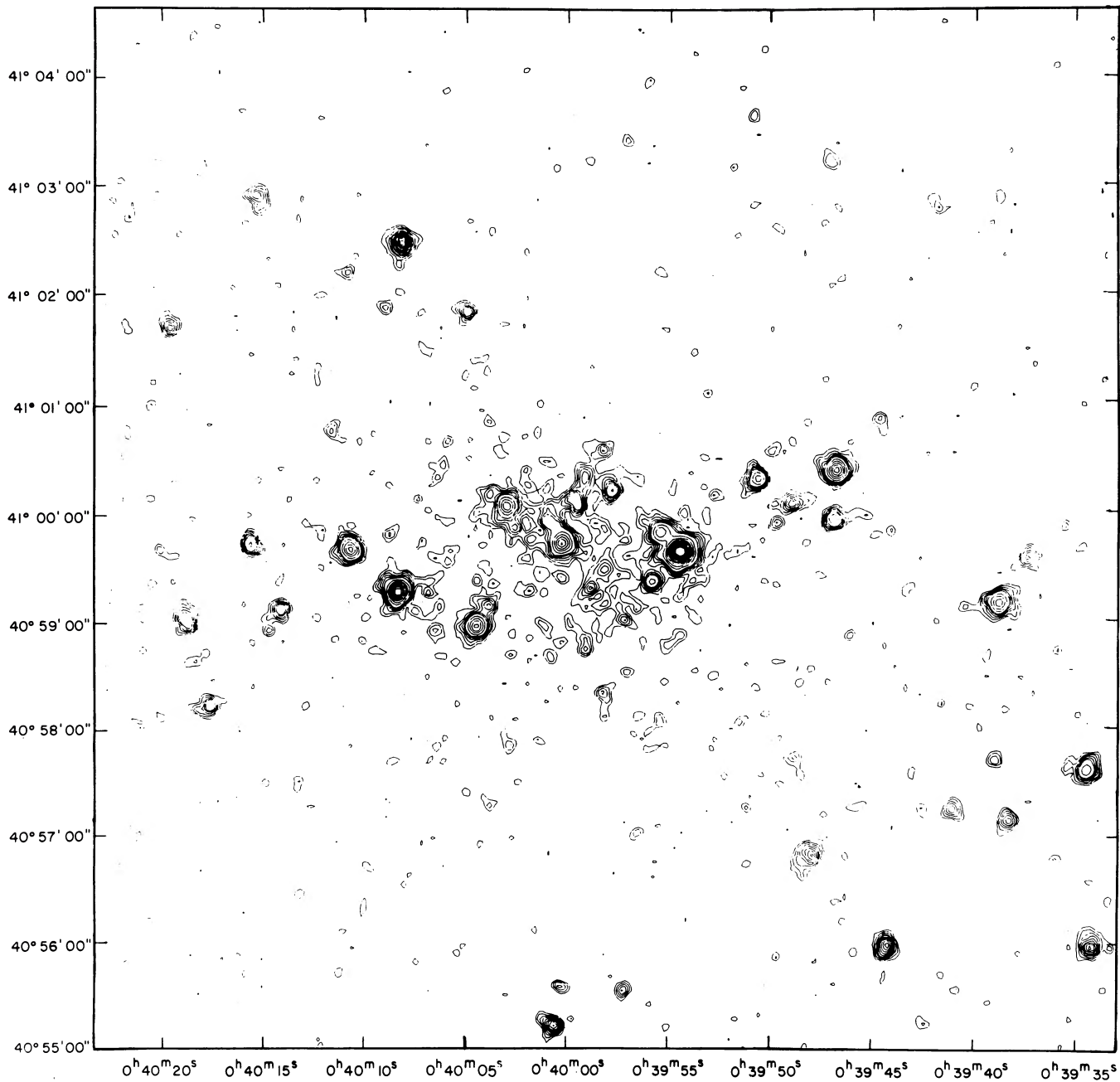
FIG. 4a

FIG. 4.—Isointensity contours of the central region of M31. (a) HRI data. The data (at the resolution of 1″ pixel^{-1}) have been smoothed with a Gaussian of $\sigma = 4''$. The first contour is at the 2 σ level over the background. (b) Broad-band IPC data. A smoothing with $\sigma = 32''$ has been applied. The dashed contour is at 0 counts arcmin^{-2}. Other contours are chosen to better illustrate the X-ray morphology.

the source counts). For very weak sources, or sources in crowded, confused regions, we have used the standard detection cell, to maximize the signal-to-noise ratio and avoid confusion, at the cost of a larger scattering correction factor ($\sim 30\%$). The background has been estimated from background templates (see above), except for a few sources close to central confused region, for which we have adapted a background estimated from the average surface brightness emission at the same galactocentric distance, to take into account the contribution from the extended bulge.

From the net counts we have derived count rates, fluxes, and luminosities (cols. [8]–[10]). Appropriate corrections for PRF, vignetting, and average field dead time were applied to obtain the corrected count rates. Fluxes were derived in the 0.2–4.0 keV band assuming a thermal bremsstrahlung spectrum with $kT = 5$ keV and $N_H = 7 \times 10^{20}$ cm^{-2} (Stark et al. 1991). A distance of 690 kpc was assumed to derive luminosities. The count rates derived for some of the sources in I573 are highly uncertain, as remarked in the notes to Table 2A. This is due to the fact that the spacecraft was not stable during this observation and only the central portion of the field was uniformly exposed as a result. An accurate estimate of the exact exposure
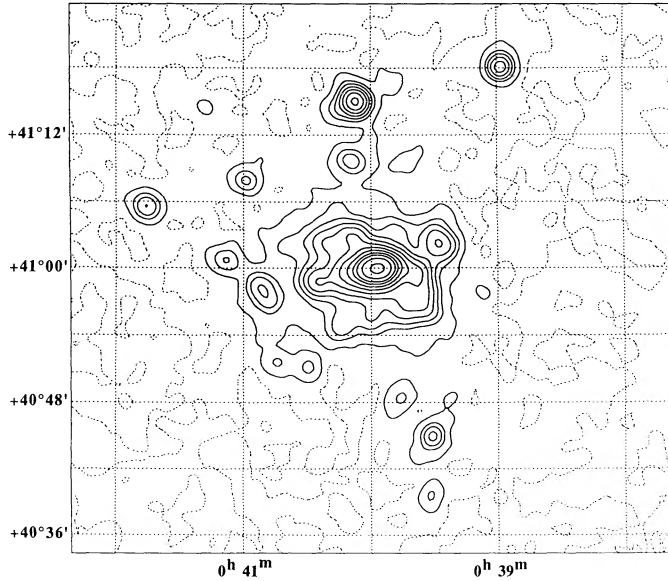
FIG. 4b

time at each point is hampered by the poor knowledge of the shadowing effects of the " ribs," which affect a larger portion of the image than in other sequences obtained in more stable telescope conditions.

For sources covered by the three central HRI fields, we also list in Table 3 the count rates in each single field.

2.4. Total X-Ray Luminosity

To estimate the total X-ray luminosity of M31 we have integrated the net observed counts in the three partially overlap-
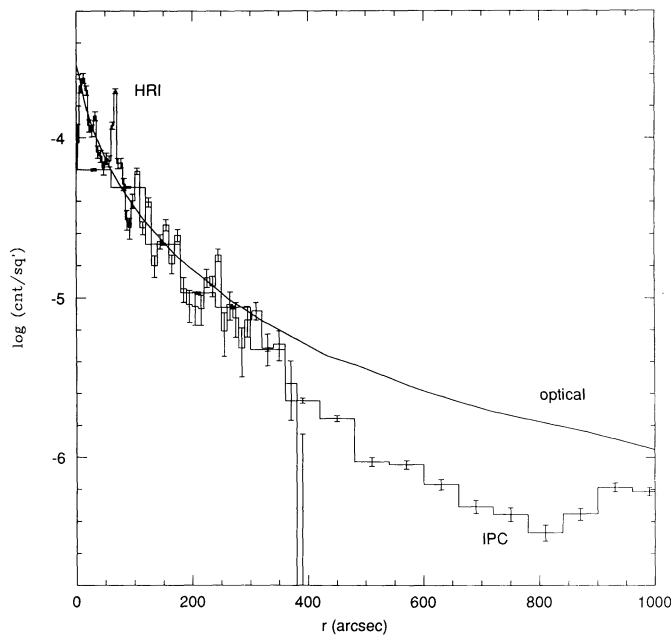
FIG. 5.—The azimuthally averaged, background-subtracted surface brightness distribution of the IPC data in the central region of M31. The data are averaged in concentric annuli centered at R.A. 00^h40^m, decl.: $41°00'$. The error bars are statistical only. The HRI data are also shown, normalized to the IPC data outside $\sim 3'$ radius. The optical profile (S. Kent, private communication) is plotted with the X-ray data. The optical profile is arbitrarily normalized to the HRI data.

ping fields I573, I574, and I575 (Fig. 1), within an ellipse of $\sim 2°5 \times 1°$ along the optical position angle of the galaxy.[1] The background level has been taken from the templates described above (see § 2.1.1). The results indicate an IPC count rate of ~ 1.15 counts s^{-1}. Assuming an average vignetting correction of $\sim 10\%$, this corresponds to an integrated flux of $\sim 5 \times 10^{-11}$ ergs cm^{-2} s^{-1} (0.2–4.0 keV), for a thermal bremsstrahlung spectrum with $kT = 5$ keV and Galactic absorption and to $L_x \sim 3 \times 10^{39}$ ergs s^{-1}, for $D = 690$ kpc. The emission is roughly equally divided between the bulge ($r \sim 5'$) and the disk of the galaxy.

The individual sources detected in the disk of M31 (i.e., the region outside $r \sim 7'$, which is the size of the central confused region seen with the IPC) account almost entirely for the emission detected in that region,. In fact, the counts within the source detection circles, corrected for the average PRF scattering, account for all of the net counts detected. However, as remarked when discussing the IPC background subtraction, we would tend to underestimate large low surface brightness features in the disk, so that the total X-ray luminosity of M31 could be somewhat underestimated also.

Within $r \sim 7'$, the IPC observations cannot resolve individual sources. However, 57 sources are individually detected with the HRI observations (see Table 2).

To estimate whether the individual sources account for all of the emission in the bulge of M31, or whether an additional component is present (see § 3.2), we have analyzed the HRI data from the merged image with the following procedure. In a circle of $r \sim 5'$ (optical size of the bulge; Morton, Andereck, & Bernard 1977), we have excluded the regions occupied by bright X-ray sources, by "punching" holes at the positions of the sources of the same size as the detection cells used ($r = 6''7$ and $18''$, containing 60% and 70% of the source counts, respectively). We have then used this result in two ways:

1. We have summed the residual emission, which amounts to 5400 counts above a background estimated in an annulus of $400''$ to $500''$ radii, and we have corrected it for the area that was covered by the sources. This gives 5800 counts within $r = 5'$.

2. We have evaluated an average of this residual emission in concentric annuli of $1'$ width and recalculated the source net counts using, as a background, the average value thus obtained appropriate for the galactocentric distance of the source. The extended emission outside of sources is then obtained by the difference between the total net counts within $r = 5'$ and the counts attributed to the individual sources. This gives $\gtrsim 5900$ counts not attributed to sources.

Both of these methods give the same result. Since no correction is applied to take into account photons scattered outside the cells used to mask the source contribution, neither in the evaluation of the background nor in the estimate of the residual emission, this value should be regarded as a conservative upper limit to the residual emission outside sources in the bulge. An average 1.4 correction for scattering from the contribution of each source (smaller than the average scattering used for the sources, to take into account photons scattered at even larger radii than the bulge size) lowers the residual counts to ~ 4300.

This estimate corresponds to a flux of $\sim 10^{-11}$ ergs cm^{-2} s^{-1} for the spectral parameters of Table 2. For a spectrum with

X-Ray Sources in M31 Detected with the *Einstein* Instruments

Source Number (1)	C84 Number (2)	R.A. (1950) (3)	Decl. (1950) (4)	Instrument (5)	Net Counts (6)	Error (7)	Corrected Count Rate (8)	$F_x (\times 10^{13})$ (0.2–4.0 keV) (c.g.s.) (9)	L_x (0.2–4.0 keV) (c.g.s.) (10)
1[a,b]	...	$0^h 36^m 51\overset{s}{.}9$	$40°19'35''$	I	18.7	8	1.51×10^{-3}	≥ 0.60	$\geq 3.47 \times 10^{36}$
2[a]	1	0 37 18.7	40 15 53.3	I	62.8	16.2	4.10×10^{-3}	≥ 1.64	$\geq 9.43 \times 10^{36}$
3	2	0 37 30.31	40 33 39.2	H	114.9	11.3	1.69×10^{-2}	25.38	1.46×10^{38}
4	3	0 37 36.88	40 27 33.2	H	71.9	9.2	1.09×10^{-2}	16.35	9.40×10^{37}
5[a]	4	0 37 42.3	40 13 23	I	32.2	9.2	2.47×10^{-3}	≥ 0.99	$\geq 5.69 \times 10^{36}$
6[c]	5	0 37 42.4	41 12 36	I	33.8	11.1	2.66×10^{-3}	1.06	...
7[a,b]	...	0 38 02.8	40 35 06	I	22.2	8.7	1.65×10^{-3}	≥ 0.66	$\geq 3.79 \times 10^{36}$
8[a]	6	0 38 40.7	40 42 34	I	54.8	15.5	4.43×10^{-3}	≥ 1.77	$\geq 1.02 \times 10^{37}$
9	7	0 38 58.99	41 17 55.1	H	98.9	12.2	5.81×10^{-3}	8.72	5.01×10^{37}
10[c]	8	0 39 08.2	40 57 38	I	57	15.5	2.25×10^{-3}	0.90	...
11[a,c]	9	0 39 08.5	40 04 57	I	355.2	20.1	3.88×10^{-2}	≥ 15.54	...
12	10	0 39 23.57	41 01 49.4	H	67	13.1	1.71×10^{-3}	2.56	1.47×10^{37}
13	12	0 39 28.8	40 22 44	I	46.6	10.7	4.09×10^{-3}	1.64	9.42×10^{36}
14[c]	13	0 39 29.11	41 02 10.3	H	87	13.8	2.15×10^{-3}	3.23	...
15[a]	14	0 39 31.3	40 03 17	I	961.8	31.7	1.22×10^{-1}	≥ 48.83	$\geq 2.81 \times 10^{38}$
16	15	0 39 31.65	40 44 49.3	H	45.8	8.8	2.59×10^{-3}	3.88	2.23×10^{37}
17	16	0 39 31.65	41 00 54.9	H	39	11.9	8.39×10^{-4}	1.26	7.24×10^{36}
18	18	0 39 32.39	40 39 27.3	H	15.3	4.4	1.11×10^{-3}	1.67	9.58×10^{36}
19	21	0 39 34.26	40 55 58.5	H	115	14.7	2.84×10^{-3}	4.26	2.45×10^{37}
20	22	0 39 34.51	40 57 37.1	H	143	15.7	3.29×10^{-3}	4.93	2.83×10^{37}
21	23	0 39 37.42	40 59 36.2	H	40	12.9	9.12×10^{-4}	1.37	7.86×10^{36}
22	25	0 39 38.37	40 57 08.8	H	44	13.1	1.06×10^{-3}	1.59	9.13×10^{36}
23	26	0 39 38.82	40 59 10.6	H	207	18.3	4.58×10^{-3}	6.88	3.95×10^{37}
24	27	0 39 39.03	40 57 43.2	H	20	6.1	5.80×10^{-4}	0.87	5.00×10^{36}
25[d]	28	0 39 41.04	40 57 14.9	H	30	12.5	6.52×10^{-4}	0.98	5.62×10^{36}
26	29	0 39 41.90	41 02 50.3	H	18	6	5.27×10^{-4}	0.79	4.54×10^{36}
27	30	0 39 44.27	40 55 58.5	H	97	15	2.25×10^{-3}	3.38	1.94×10^{37}
28	31	0 39 44.51	40 48 10.9	H	35.8	8.3	2.05×10^{-3}	3.07	1.76×10^{37}
29[d]	32	0 39 44.66	41 00 52.5	H	16	5.8	4.68×10^{-4}	0.70	4.04×10^{36}
30	33	0 39 45.6	41 09 35	I	31	8.6	4.28×10^{-3}	1.71	9.84×10^{36}
31	35	0 39 46.75	41 00 24.3	H	273	20	5.93×10^{-3}	8.90	5.11×10^{37}
32	36	0 39 46.89	40 59 57.2	H	111	15.5	2.41×10^{-3}	3.62	2.08×10^{37}
33	37	0 39 47.09	41 03 17.7	H	18	6	5.50×10^{-4}	0.83	4.74×10^{36}
34	39	0 39 47.98	40 56 49.6	H	90	14.7	2.03×10^{-3}	3.05	1.75×10^{37}
35[c,e]	40	0 39 48.89	41 00 05.4	H	41	7.6	1.14×10^{-3}	1.72	...
36[e]	...	0 39 49.78	40 59 59.4	H	21	6.2	5.97×10^{-4}	0.90	5.15×10^{36}
37	41	0 39 50.3	40 48 08	I	46	15	6.52×10^{-3}	2.61	1.50×10^{37}
38	42	0 39 50.3	41 16 22	I	75.9	14.3	3.91×10^{-3}	1.56	8.99×10^{36}
39	...	0 39 50.61	41 00 20.5	H	92	10.4	2.59×10^{-3}	3.89	2.24×10^{37}
40[d]	44	0 39 54.14	41 13 45.3	H	21.9	8.6	1.06×10^{-3}	1.59	9.15×10^{36}
41	...	0 39 54.38	40 59 39.5	H	1265	37.3	2.75×10^{-2}	41.28	2.37×10^{38}
42[f]	...	0 39 55.29	40 58 03.7	H	<33.4	...	$<9.41 \times 10^{-4}$	<1.41	$<8.11 \times 10^{36}$
43	...	0 39 55.32	40 59 50.1	H	140	12.6	3.94×10^{-3}	5.92	3.40×10^{37}
44	...	0 39 55.68	40 59 23.3	H	65	9.1	1.83×10^{-3}	2.75	1.58×10^{37}
45	51	0 39 57.11	40 59 01.1	H	24	6.4	7.15×10^{-4}	1.07	6.17×10^{36}
46	...	0 39 57.15	40 55 34.2	H	20	6.1	5.80×10^{-4}	0.87	5.00×10^{36}
47	...	0 39 57.79	41 00 13.3	H	60	8.8	1.69×10^{-3}	2.54	1.46×10^{37}
48	...	0 39 58.04	40 58 20.1	H	23	6.4	6.48×10^{-4}	0.97	5.59×10^{36}
49[e]	...	0 39 58.07	40 59 29.0	H	43	7.8	1.29×10^{-3}	1.94	1.11×10^{37}
50[e]	...	0 39 58.22	41 00 35.0	H	29	6.8	8.17×10^{-4}	1.23	7.05×10^{36}
51[g]	60	0 39 58.31	40 35 29.6	H	106.8	11.8	6.11×10^{-3}	9.16	5.27×10^{37}
52[e]	...	0 39 58.72	40 59 19.4	H	39	7.5	1.08×10^{-3}	1.62	9.29×10^{36}
53	...	0 39 58.97	40 58 45.8	H	23	6.4	6.54×10^{-4}	0.98	5.64×10^{36}
54[e]	...	0 39 59.08	41 00 19.7	H	43	7.8	1.21×10^{-3}	1.82	1.04×10^{37}
55	...	0 39 59.52	41 00 07.3	H	75	9.6	2.21×10^{-3}	3.32	1.91×10^{37}
56[e]	...	0 40 00.19	40 59 43.6	H	221	15.5	6.04×10^{-3}	9.07	5.21×10^{37}
57[e]	...	0 40 00.53	40 59 52.7	H	96	10.6	2.73×10^{-3}	4.09	2.35×10^{37}
58	67	0 40 00.68	40 55 13.6	H	48	13.2	1.06×10^{-3}	1.59	9.17×10^{36}
59	...	0 40 02.56	40 59 52.6	H	40	7.6	1.20×10^{-3}	1.81	1.04×10^{37}
60	...	0 40 02.90	41 00 04.6	H	160	13.3	4.72×10^{-3}	7.08	4.07×10^{37}
61	...	0 40 03.76	40 59 08.5	H	40	7.6	1.20×10^{-3}	1.81	1.04×10^{37}
62	73	0 40 04.01	41 08 59.0	H	38.9	9.5	2.29×10^{-3}	3.44	1.98×10^{37}
63	...	0 40 04.35	40 58 57.3	H	180	14.1	5.36×10^{-3}	8.04	4.62×10^{37}
64	...	0 40 04.99	41 01 51.5	H	43	7.8	1.24×10^{-3}	1.85	1.07×10^{37}
65	...	0 40 06.20	40 58 54.1	H	18	6	5.42×10^{-4}	0.81	4.67×10^{36}
66	...	0 40 06.70	40 59 18.0	H	22	6.3	6.08×10^{-4}	0.91	5.24×10^{36}
67	79	0 40 07.48	41 14 44.3	H	155.9	14.4	7.97×10^{-3}	11.95	6.87×10^{37}
68	...	0 40 08.14	41 02 29.5	H	168	17.2	3.76×10^{-3}	5.64	3.24×10^{37}
69	...	0 40 08.26	40 59 15.8	H	504	25.1	1.19×10^{-2}	17.86	1.03×10^{38}
70	...	0 40 10.1	41 09 31	I	218	19.8	9.42×10^{-3}	3.77	2.17×10^{37}
71	...	0 40 10.65	40 59 39.7	H	212	18.4	4.88×10^{-3}	7.32	4.21×10^{37}

Source Number (1)	C84 Number (2)	R.A. (1950) (3)	Decl. (1950) (4)	Instrument (5)	Net Counts (6)	Error (7)	Corrected Count Rate (8)	$F_x(\times 10^{13})$ (0.2–4.0 keV) (c.g.s.) (9)	L_x (0.2–4.0 keV) (c.g.s.) (10)
72[d]	...	0 40 11.60	41 00 45.6	H	17	5.9	5.11×10^{-4}	0.77	4.41×10^{36}
73	86	0 40 13.66	40 54 42.2	H	90	14.7	2.09×10^{-3}	3.13	1.80×10^{37}
74	...	0 40 14.09	40 59 05.4	H	59	13.6	1.39×10^{-3}	2.09	1.20×10^{37}
75	88	0 40 14.16	40 52 02.3	H	104	14.4	2.68×10^{-3}	4.02	2.31×10^{37}
76	89	0 40 15.30	41 02 55.4	H	47	13.2	1.09×10^{-3}	1.64	9.40×10^{36}
77	90	0 40 15.56	40 59 41.3	H	60	13.7	1.41×10^{-3}	2.11	1.21×10^{37}
78	91	0 40 17.52	40 58 11.8	H	52	13.4	1.15×10^{-3}	1.73	9.93×10^{36}
79	92	0 40 18.69	40 58 59.1	H	75	9.6	2.18×10^{-3}	3.26	1.88×10^{37}
80	93	0 40 19.55	41 01 42.1	H	42	7.7	1.28×10^{-3}	1.92	1.10×10^{37}
81[a,c,d]	96	0 40 23.3	40 31 55	I	20.1	8.1	2.60×10^{-3}	≥1.04	...
82[f]	97	0 40 25.38	41 02 34.3	H	<53	...	$<1.35 \times 10^{-3}$	<2.03	1.17×10^{37}
83	98	0 40 26.21	40 58 27.5	H	220	18	5.01×10^{-3}	7.51	4.32×10^{37}
84	99	0 40 27.16	41 01 43.4	H	50	12.4	1.32×10^{-3}	1.99	1.14×10^{37}
85	100	0 40 30.15	40 50 58.3	H	41	9	2.85×10^{-3}	4.27	2.45×10^{37}
86[h]	...	0 40 34.3	41 42 50	I	34.9	10.5	2.39×10^{-3}	≥0.96	≥5.49×10^{36}
87	101	0 40 34.50	41 03 54.4	H	52	12.5	1.43×10^{-3}	2.15	1.24×10^{37}
88	102	0 40 38.8	41 01 46	I	79.2	20.3	3.27×10^{-3}	1.31	7.53×10^{36}
89	103	0 40 43.56	41 02 08.1	H	25.9	6.3	1.66×10^{-3}	2.48	1.43×10^{37}
90	104	0 40 43	40 51 22	I	95	16.3	4.11×10^{-3}	1.64	9.44×10^{36}
91[c]	105	0 40 49.98	40 57 04.2	H	62	10.1	4.16×10^{-3}	6.24	...
92	106	0 40 52.96	40 58 23.8	H	46.9	8.9	3.15×10^{-3}	4.73	2.72×10^{37}
93	107	0 40 59.97	41 07 48.1	H	30.9	8	1.91×10^{-3}	2.86	1.64×10^{37}
94	108	0 41 09.11	41 00 33.2	H	45.9	8.8	2.70×10^{-3}	4.05	2.33×10^{37}
95[i]	...	0 41 13	40 30 07	I	21.5	6.5	4.09×10^{-3}	1.64	9.41×10^{36}
96	109	0 41 18.74	41 14 15.4	H	28.9	7.8	2.33×10^{-3}	3.50	2.01×10^{37}
97	112	0 41 44.78	41 05 13.8	H	84.9	10.8	5.73×10^{-3}	8.59	4.94×10^{37}
98[d,i]	...	0 42 12	40 43 34	I	31.1	10.9	5.16×10^{-3}	2.07	1.19×10^{37}
99[h]	...	0 42 28.3	41 20 40	I	45	12	2.57×10^{-3}	≥1.03	≥5.91×10^{36}
100	...	0 42 37.5	41 29 13	I	38.2	12.6	1.78×10^{-3}	0.71	4.10×10^{36}
101	113	0 42 54.94	41 51 41.6	H	62.4	10.7	3.33×10^{-3}	4.99	2.87×10^{37}
102	114	0 43 00.49	41 23 21.9	H	197.6	14.4	2.88×10^{-2}	43.18	2.48×10^{38}
103	...	0 43 24.2	41 52 17	I	42.2	10.7	2.37×10^{-3}	0.95	5.46×10^{36}
104[h]	115	0 43 37.9	41 48 26	I	391.9	22	2.14×10^{-2}	≥8.56	≥4.92×10^{37}
105	116	0 43 41.38	41 45 30.0	H	67.4	10.9	3.68×10^{-3}	5.52	3.17×10^{37}
106	...	0 43 42.6	41 31 30	I	34	10.7	1.78×10^{-3}	0.71	4.10×10^{36}
107[h,j]	...	0 44 15.0	42 04 25	I	87.9	13.1	8.86×10^{-3}	≥3.54	≥2.04×10^{37}
108[h]	...	0 45 14.2	41 24 37	I	108.8	21.6	1.11×10^{-2}	≥4.46	≥2.56×10^{37}

[a] Sources in I573, in regions where the exposure is much smaller than at the field center. The flux is uncertain due to the nonuniform exposure, and it is probably underestimated.

[b] Detected in the IPC hard band only. The count rates in the table are from the broad band.

[c] Identified with a foreground/background object (Crampton et al. 1984). Source 11 is 5C 3.100 (Mkn 957) (Halpern & Oke 1987). Source 15 is the Seyfert 1 galaxy IV Zw 29 (Zwicky et al. 1970; Grandi & Osterbrock 1978).

[d] These sources, below the 3 σ threshold, are included in the list because they are either detected by the standard detect algorithm and/or they are clearly visible in contour maps.

[e] Contamination from the counts of a nearby source. The detection cell of these sources contains counts also attributed to another source. The pairs of sources are (35, 36), (49, 52), (50, 54), (56, 57).

[f] These sources were not detected in the merged HRI exposure (see text) but are above threshold in one field (H579) with $f_x = 1.7 \times 10^{-13}$ and $f_x = 3.16 \times 10^{-13}$ ergs cm^{-2} s^{-1} for sources 42 and 82, respectively. These sources are not used in the following analysis.

[g] M32.

[h] Fluxes for sources near the IPC support structure ("ribs") are probably underestimated due to the shadowing effects of the structure.

[i] Sources in X-ray fields not analyzed previously.

[j] This source is probably composed of two sources with <2′ angular separation.

TABLE 2B

X-Ray Sources in Crampton et al. (1984) Not Detected in Our Analysis

Source Number (1)	C84 Number (2)	R.A. (1950) (3)	Decl. (1950) (4)	Instrument (5)	Net Counts (6)	Error (7)	Corrected Count Rate (8)	$F_x(\times 10^{13})$ (0.2–4.0 keV) (c.g.s.) (9)	L_x (0.2–4.0 keV) (c.g.s.) (10)
1b	11	00^{h}39^{m}25^{s}42	41°12′24″8	H	18	8.3	$\sim9.02 \times 10^{-4}$	~1.35	~7.78×10^{36}
2b	20	00 39 34.04	40 46 44	H	17	7	$\sim8.56 \times 10^{-4}$	~1.28	~7.38×10^{36}
3b	24	00 39 37.95	40 42 59.7	H	17	7	$\sim8.56 \times 10^{-4}$	~1.28	~7.38×10^{36}
4b	38	00 39 47.79	41 26 08.0	H	16	8	$\sim1.15 \times 10^{-3}$	~1.72	~9.93×10^{36}
5b	66	00 40 00.27	40 55 35.9	H	14	6	$\sim4.21 \times 10^{-4}$	~0.63	~3.63×10^{36}
6b[a]	78	00 40 07.22	40 49 44.6	H	18	7	$\sim1.30 \times 10^{-3}$	~1.94	...
7b	110	00 41 34.17	41 06 01.9	H	13	6.8	$\sim7.85 \times 10^{-4}$	~1.17	~6.77×10^{36}
8b[a]	111	00 41 39.49	41 14 38.5	H	17	7	$\sim1.53 \times 10^{-3}$	~2.30	...

[a] Sources in I573, in regions where the exposure is much smaller than at the field center. The flux is uncertain due to the nonuniform exposure, and it is probably underestimated.

89
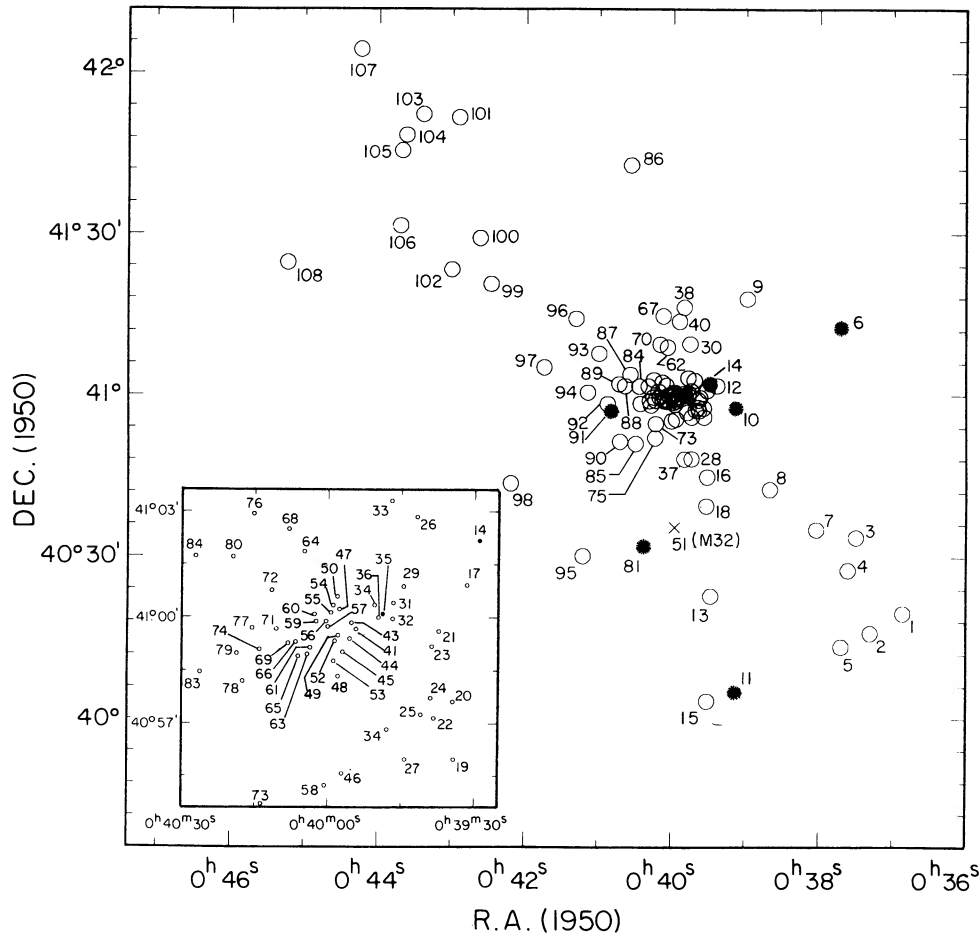
Fig. 6.—Spatial distribution of the sources in M31. Filled dots identify foreground sources (from Crampton et al. 1984). The X identifies a source at the position of M32.

$kT = 1$ keV, more appropriate for gaseous emission, $f_x \sim 7 \times 10^{-12}$ ergs cm^{-2} s^{-1}.

2.5. Variability

Table 3 shows the comparison of count rates for the sources included in common to the three central HRI fields. Two sources detected in all three observations (sources 41 and 56) appear to vary at a >3 σ confidence level. In a few other cases, the source was detected only in one or two of the HRI fields, and the upper limits seem to be inconsistent with the detections. To evaluate this quantitatively, a Poisson probability that the source has varied has been calculated, following Maccacaro, Garilli, & Mereghetti (1987; see also Trinchieri, Fabbiano, & Romaine 1990). Assuming a threshold probability $P = 5 \times 10^{-4}$ below which the flux is assumed to vary, nine more sources (sources 23, 31, 39, 46, 47, 53, 60, 71, and 78) are not constant at this significance. Typically, the flux variations are of a factor of 1.5–3, except for source 56, where a flux decrease of up to a factor of 12 between maximum and minimum flux is observed.

A more complete comparison between all sources in the M31 fields covered by more than one observation has been attempted by comparing the individual fluxes in each field. In Table 4 we list the three sources found to vary in these comparisons. However, this comparison can only be done for those sources that are not in confused regions and that are far from

the regions of obscuration. One field (I573) for which the actual exposure is poorly known (see above, see also Collura et al. 1990) has not been used in the comparison. In a comparison between IPC count rates, only source 70 shows an intensity variation. Two additional sources (sources 67 and 85) present flux variations between IPC and HRI data.

In addition to these, sources 16 and 101 were found to vary on time scales of ~ 6000 and > 7000 s, respectively, by Collura et al. (1990; their sources 4I and 25I). A light curve consistent with those of Galactic low-mass binaries, with a period of $\sim 3.25 \times 10^4$ s was found for source 16, identified with a gobular cluster by Crampton et al. (1984). Less convincing evidence of a periodicity was found for source 101, identified with a blue star.

2.6. Source Spectra

The moderate energy resolution of the IPC can be used to evaluate the spectral parameters of the detected sources. The bulge sources cannot be resolved spatially by the IPC and appear as a diffuse emission region. The spectral analysis of this region shows that the emission is dominated by low-mass binaries with no intrinsic absorption cutoff (Fabbiano, Trinchieri, & Van Speybroeck 1987). In this paper we report the results of the spectral analysis of individually detected IPC sources, situated outside the inner bulge of M31. These sources lay outside the 4' × 4' central region of the IPC field, in which

TABLE 3

COMPARISON OF CORRECTED COUNT RATES IN THE THREE CENTRAL HRI FIELDS

SOURCE NUMBER	R.A.	DECL.	H579 Count Rate[a]	H579 Error	H4479 Count Rate[a]	H4479 Error	H7066 Count Rate[a]	H7066 Error	VARIABLE?
12	$00^h39^m23^s.57$	$41°01'49''.4$	1.43×10^{-3}	3.80×10^{-4}	1.48×10^{-3}	4.14×10^{-4}	$<1.30 \times 10^{-3}$	...	
19	00 39 29.11	41 02 10.3	2.52×10^{-3}	4.62×10^{-4}	2.26×10^{-3}	4.77×10^{-4}	$<3.80 \times 10^{-3}$	...	
20	00 39 34.51	40 57 37.1	3.69×10^{-3}	5.31×10^{-4}	2.87×10^{-3}	4.98×10^{-4}	$<1.79 \times 10^{-3}$	...	
21	00 39 37.42	40 59 36.2	1.52×10^{-3}	3.76×10^{-4}	1.31×10^{-3}	3.58×10^{-4}	$<1.38 \times 10^{-3}$	...	
22	00 39 38.37	40 57 08.8	1.02×10^{-3}	3.35×10^{-4}	1.52×10^{-3}	4.01×10^{-4}	$<3.01 \times 10^{-3}$	...	
23	00 39 38.82	40 59 10.6	6.30×10^{-3}	6.79×10^{-4}	3.69×10^{-3}	5.41×10^{-4}	$<2.22 \times 10^{-3}$	...	Yes
25	00 39 41.04	40 57 14.9	2.06×10^{-3}	4.10×10^{-4}	$<7.38 \times 10^{-4}$	...	$<1.08 \times 10^{-3}$	...	
27	00 39 44.27	40 55 58.5	3.47×10^{-3}	5.33×10^{-4}	2.15×10^{-3}	4.41×10^{-4}	$<2.33 \times 10^{-3}$	...	
29	00 39 44.66	41 00 52.5	$<5.08 \times 10^{-4}$	...	1.23×10^{-3}	3.51×10^{-4}	$<1.37 \times 10^{-3}$	...	
31	00 39 46.75	41 00 24.3	$<1.20 \times 10^{-3}$	...	$<5.17 \times 10^{-4}$	...	3.97×10^{-2}	2.71×10^{-3}	Yes
32	00 39 46.89	40 59 57.2	2.05×10^{-3}	4.10×10^{-4}	2.76×10^{-3}	4.77×10^{-4}	2.43×10^{-3}	7.60×10^{-4}	
34	00 39 47.98	40 56 49.6	1.58×10^{-3}	3.79×10^{-4}	2.24×10^{-3}	4.41×10^{-4}	2.62×10^{-3}	8.20×10^{-4}	
35[b]	00 39 48.89	41 00 05.4	1.83×10^{-3}	3.90×10^{-4}	$<1.64 \times 10^{-3}$	...	$<1.60 \times 10^{-3}$	...	
36[b]	00 39 49.78	40 59 59.4	9.33×10^{-4}	3.08×10^{-4}	$<1.26 \times 10^{-3}$	...	$<1.34 \times 10^{-3}$	...	
39	00 39 50.61	41 00 20.5	6.71×10^{-3}	6.92×10^{-4}	$<2.99 \times 10^{-4}$	...	$<9.40 \times 10^{-4}$	...	Yes
41	00 39 54.38	40 59 39.5	2.96×10^{-2}	1.42×10^{-3}	2.88×10^{-2}	1.48×10^{-3}	9.66×10^{-3}	1.35×10^{-3}	Yes
42	00 39 55.29	40 58 03.7	1.08×10^{-3}	3.17×10^{-4}	$<5.02 \times 10^{-4}$	...	$<1.05 \times 10^{-3}$	...	
43	00 39 55.32	40 59 50.1	4.64×10^{-3}	5.84×10^{-4}	4.56×10^{-3}	5.93×10^{-4}	$<2.72 \times 10^{-3}$	...	
44	00 39 55.68	40 59 23.3	1.28×10^{-3}	3.36×10^{-4}	2.11×10^{-3}	4.16×10^{-4}	$<2.38 \times 10^{-3}$	...	
46	00 39 57.15	40 55 34.2	$<3.56 \times 10^{-4}$	...	1.87×10^{-3}	4.10×10^{-4}	$<1.12 \times 10^{-3}$	...	Yes
47	00 39 57.79	41 00 13.3	3.41×10^{-3}	5.00×10^{-4}	$<8.11 \times 10^{-4}$	...	$<2.90 \times 10^{-3}$	...	Yes
48	00 39 58.04	40 58 20.1	1.02×10^{-3}	3.10×10^{-4}	$<1.30 \times 10^{-3}$	...	$<1.05 \times 10^{-3}$	...	
49	00 39 58.07	40 59 29.0	1.41×10^{-3}	3.48×10^{-4}	1.34×10^{-3}	3.68×10^{-4}	$<2.33 \times 10^{-3}$	...	
50	00 39 58.22	41 00 35.0	1.18×10^{-3}	3.33×10^{-4}	$<1.44 \times 10^{-3}$	...	$<1.61 \times 10^{-3}$	...	
52	00 39 58.72	40 59 19.4	1.48×10^{-3}	3.57×10^{-4}	$<1.41 \times 10^{-3}$	...	$<3.18 \times 10^{-3}$	...	
53	00 39 58.97	40 58 45.8	$<7.24 \times 10^{-4}$	...	$<1.05 \times 10^{-3}$	...	3.76×10^{-3}	9.13×10^{-4}	Yes
54	00 39 59.08	41 00 19.7	1.55×10^{-3}	3.60×10^{-4}	1.30×10^{-3}	3.42×10^{-4}	$<1.86 \times 10^{-3}$	...	
55	00 39 59.52	41 00 07.3	2.98×10^{-3}	4.93×10^{-4}	2.20×10^{-3}	4.42×10^{-4}	$<2.29 \times 10^{-3}$	...	
56	00 40 00.19	40 59 43.6	1.12×10^{-2}	8.69×10^{-4}	9.48×10^{-4}	3.06×10^{-4}	5.54×10^{-3}	1.05×10^{-3}	Yes
57	00 40 00.53	40 59 52.7	2.14×10^{-3}	4.13×10^{-4}	2.13×10^{-3}	4.36×10^{-4}	3.21×10^{-3}	8.56×10^{-4}	
58	00 40 00.68	40 55 13.6	2.17×10^{-3}	4.24×10^{-4}	1.45×10^{-3}	3.69×10^{-4}	$<2.80 \times 10^{-3}$	...	
59	00 40 02.56	40 59 52.6	1.34×10^{-3}	3.42×10^{-4}	1.36×10^{-3}	3.48×10^{-4}	$<9.12 \times 10^{-4}$	...	
60	00 40 02.90	41 00 04.6	6.06×10^{-3}	6.76×10^{-4}	5.68×10^{-3}	6.72×10^{-4}	$<1.14 \times 10^{-3}$	...	Yes
61	00 40 03.76	40 59 08.5	1.74×10^{-3}	3.77×10^{-4}	$<1.50 \times 10^{-3}$	...	$<2.13 \times 10^{-3}$	...	
63	00 40 04.35	40 58 57.3	6.82×10^{-3}	7.18×10^{-4}	4.76×10^{-3}	5.98×10^{-4}	3.00×10^{-3}	8.55×10^{-4}	
64	00 40 04.99	41 01 51.5	2.22×10^{-3}	4.29×10^{-4}	$<1.06 \times 10^{-3}$	...	$<1.65 \times 10^{-3}$	...	
68	00 40 08.14	41 02 29.5	3.75×10^{-3}	5.39×10^{-4}	4.18×10^{-3}	5.73×10^{-4}	3.65×10^{-3}	9.12×10^{-4}	
69	00 40 08.26	40 59 15.8	1.43×10^{-2}	1.04×10^{-3}	9.38×10^{-3}	8.22×10^{-4}	9.36×10^{-3}	1.42×10^{-3}	
71	00 40 10.10	40 59 39.7	5.53×10^{-3}	6.65×10^{-4}	6.48×10^{-3}	6.90×10^{-4}	$<4.05 \times 10^{-3}$	...	Yes
73	00 40 13.66	40 54 42.2	2.09×10^{-3}	4.29×10^{-4}	3.64×10^{-3}	5.48×10^{-4}	$<2.70 \times 10^{-3}$	...	
74	00 40 14.09	40 59 05.4	2.37×10^{-3}	4.58×10^{-4}	1.14×10^{-3}	3.51×10^{-4}	$<2.96 \times 10^{-3}$	...	
75	00 40 14.16	40 52 02.3	2.22×10^{-3}	4.65×10^{-4}	2.33×10^{-3}	4.82×10^{-4}	$<2.37 \times 10^{-3}$	...	
76	00 40 15.30	41 02 55.4	1.34×10^{-3}	3.63×10^{-4}	1.17×10^{-3}	3.46×10^{-4}	$<3.44 \times 10^{-3}$	...	
77	00 40 15.56	40 59 41.3	2.49×10^{-3}	4.72×10^{-4}	1.44×10^{-3}	3.58×10^{-4}	$<2.94 \times 10^{-3}$	...	
78	00 40 17.52	40 58 11.8	3.92×10^{-3}	5.47×10^{-4}	$<7.41 \times 10^{-4}$	...	$<5.53 \times 10^{-4}$	...	Yes
79	00 40 18.69	40 58 59.1	2.34×10^{-3}	4.43×10^{-4}	2.41×10^{-3}	4.49×10^{-4}	$<3.08 \times 10^{-3}$	...	
80	00 40 19.55	41 01 42.1	1.15×10^{-3}	3.51×10^{-4}	1.42×10^{-3}	3.76×10^{-4}	$<1.74 \times 10^{-3}$	...	
82	00 40 25.38	41 02 34.3	1.47×10^{-3}	3.89×10^{-4}	$<3.51 \times 10^{-4}$	...	$<1.29 \times 10^{-3}$	...	
83	00 40 26.21	40 58 27.5	4.95×10^{-3}	6.13×10^{-4}	4.37×10^{-3}	5.90×10^{-4}	3.00×10^{-3}	8.32×10^{-4}	
84	00 40 27.16	41 01 43.4	1.78×10^{-3}	4.30×10^{-4}	1.18×10^{-3}	3.74×10^{-4}	$<3.11 \times 10^{-3}$	...	
87	00 40 34.50	41 03 54.4	$<9.98 \times 10^{-4}$	...	2.29×10^{-3}	4.95×10^{-4}	$<2.89 \times 10^{-3}$	...	

[a] The source counts are derived all from a circle corresponding to the detection cell size (radius = 6".7).
[b] Partially overlapping detection circles.

TABLE 4

COMPARISON OF HRI AND IPC FLUXES

SOURCE NUMBER	HRI FLUX ($\times 10^{-13}$)	IPC FLUX ($\times 10^{-13}$) I574	IPC FLUX ($\times 10^{-13}$) I4490
67	11.95 ± 1.10	22.18 ± 0.71	19.91 ± 1.13
70	...	3.77 ± 0.33	8.52 ± 0.76
85	4.27 ± 0.93	1.72 ± 0.28	3.72 ± 0.59

NOTE.—HRI sequence H4486 for source 67 and H579 for source 85.

the detector gain is well calibrated. Therefore one must proceed with caution in evaluating spectral parameters, due to possible systematic errors caused by spatial variations of the instrumental gain across the field of view when evaluating the spectral parameters.

We have followed two different approaches. We have used a χ^2 two-parameter fit to a thermal bremsstrahlung spectrum with low-energy cutoff to evaluate the spectral parameters of all sources detected with ≥ 200 net counts in a standard 3' source circle. For one of these sources (source 93) we have also analyzed a second observation yielding only 90 counts. We have then extended the analysis to include all sources with

≥ 100 counts by using X-ray colors (Kim, Fabbiano, & Trinchieri 1991). Sources that are confused (for example, sources 91 and 92 are not resolved in the IPC observations) or that are too close to the bulge emission have not been included.

2.6.1. *Spectral Fits*

We have performed a two parameter spectral analysis on the 14 sources listed in Table 5. Five of these sources were detected in two different IPC fields, and each field was analyzed separately. In all cases, the source counts were extracted from circles of 3' radius centered on the X-ray centroid, and the background was evaluated from circles of radius 6'.7, centered off-square in source-free areas at a comparable distance from the field center. Because of the spread of the IPC PRF, the source circles used in the spectral analysis contain more counts than the cells used for source detection listed in Table 2. The detection cells are chosen to optimize the signal-to-noise ratio in the case of faint sources, while the larger circle used for the count extraction in the spectral analysis aims at maximizing the signal-to-noise ratio in the case of strong sources. Table 5 gives the source numbers; the IPC sequence numbers; the time-averaged instrumental gain; the spectral channels used for the fit (the IPC data are binned in 16 spectral channels; the energy boundaries vary as a function of the instrumental gain); the net counts used for the spectral analysis from each IPC field with their statistical error; the best-fit χ^2 and degrees of freedom; the 90% confidence regions for the two interesting parameters N_H and kT; and the N_H in M31 at each source position, estimated from published H I maps. The 68%, 90%, and 99% confidence contours for all the sources fitted with the nominal IPC gain are shown in Figure 7. Two of the IPC sequences (I574 and I575) were obtained when the IPC gain was not stable but was increasing continuously during the observation. For these sequences we have estimated the time history of the

detector gain at the source position and used it in the spectral model.

As mentioned above, the sources used for the spectral analysis fall outside the well-calibrated area of the IPC field. In this case, the uncertainty in the gain could be as much as ± 1 (F. R. Harnden, Jr. 1990, private communication; gain values range from ~ 12 to ~ 25; see Table 5). The five sources observed in two different IPC fields give us a way to estimate directly the effect of the spatial variations of the gain. These sources fall at different positions in the detector and were therefore observed at different average instrumental gains. The results of the spectral fits are similar for each source (see Table 5), while the expected gain uncertainty would result in a larger variation in the results (see Fig. 8). To be conservative, however, we have still considered the possibility that the nominal gain was in error by as much as ± 1 for sources observed only once, whenever the confidence contours suggested an N_H above the line of sight value of the H I column in M31. We have then also evaluated the confidence regions of the spectral parameters at the outermost values obtained from these extreme gain values. These estimates are given in Table 5 in parentheses. Figure 8a shows the 90% contours for source 4 obtained by using the nominal gain and the ± 1 values. For comparison the 90% contours of source 62, obtained by fitting the two separate observations at the nominal gain, are shown in Figure 8b.

Figure 7 and Table 5 show that the temperatures are not well constrained, with the exception of sources 67 and 104, with very low emission temperatures ($kT \sim 0.5$-1.5 keV), and source 101, which is instead very hard ($kT > 4.5$ keV). Eight sources (sources 3, 4, 9, 67, 93, 102, 104, and 105) have large low energy cutoffs, higher than or barely consistent with the Galactic line-of-sight absorption ($N_H \sim 7 \times 10^{20}$ cm^{-2}; Stark et al. 1991), and higher than measured in the bulge assuming the

TABLE 5

RESULTS OF SPECTRAL FITS

SOURCE NUMBER	SEQUENCE NUMBER	IPC GAIN	SPECTRAL CHANNEL	NET COUNTS	90% CONFIDENCE REGIONS		log N_H IN M31[a] (cm^{-2})	$\chi^2(\nu)$
					kT(keV)	log N_H(cm^{-2})		
3.........	573	14.7 (13.8–15.8)	2–12	933 ± 34	>2	21.3–21.6 (20.9–22.0)	21.4	8.2(8)
4.........	573	14.8 (13.8–15.8)	2–12	646 ± 30	>1	21–22 (20.8–22.0)	21.4	11.6(8)
9.........	574	18.2 (17.2–19.2)	2–12	453 ± 34	...	21.8–22.6 (21.6–22.7)	21.1	5.5(8)
11.........	573	15.4	2–12	507 ± 28	>1	<21	21.0	12.8(8)
15.........	573	15.1	2–12	1304 ± 39	>1.3	20.7–21.5	21.0	7.2(8)
51.........	573	15.5	2–12	244 ± 22	>0.75	20.2–21.8	21.4	12.8(8)
62.........	574	19.4	2–12	536 ± 35	>1	20.3–21.7	21.2	8.1(8)
	4490	11.6	2–10	328 ± 23	>1.5	20.6–21.8		11.6(6)
67.........	574	18.8	2–12	1405 ± 46	1–2	21.5–21.8	21.5	6.4(8)
	4490	13.0	2–10	488 ± 26	>1	21.5–22.2		3.1(6)
	574	19.2	2–12	476 ± 34	>1	20.2–21.5	21.1	9.8(8)
	4490	11.8	2–10	314 ± 23	>1.3	20.7–21.7		12.9(6)
93.........	574	20.2	2–12	239 ± 30	...	21.4–22.8	21.0	5.6(8)
	4490	12.4	2–10	90 ± 16	...	20.2–22.5		5.0(6)
94.........	574	20.5	2–12	325 ± 32	>1	20.3–21.8	21.6	8.8(8)
	4490	12.4	2–10	168 ± 18		<22		15.3(6)
102.........	575	24.8 (23.8–25.8)	4–14	1685 ± 46	>4	21.4–21.8 (21.3, >22.0)	21.5	16.4(8)
104.........	675	23.9	4–14	401 ± 29	0.4–1.8	21.8–22.5	21.4	3.4(8)
105.........	575	24.2	4–14	304 ± 28	...	21.2–22.5	21.4	4.8(8)

[a] Estimated from the plots in Emerson 1974 and Unwin 1980a, b. The log of the line-of-sight Galactic column density is 20.8 (Stark et al. 1991).
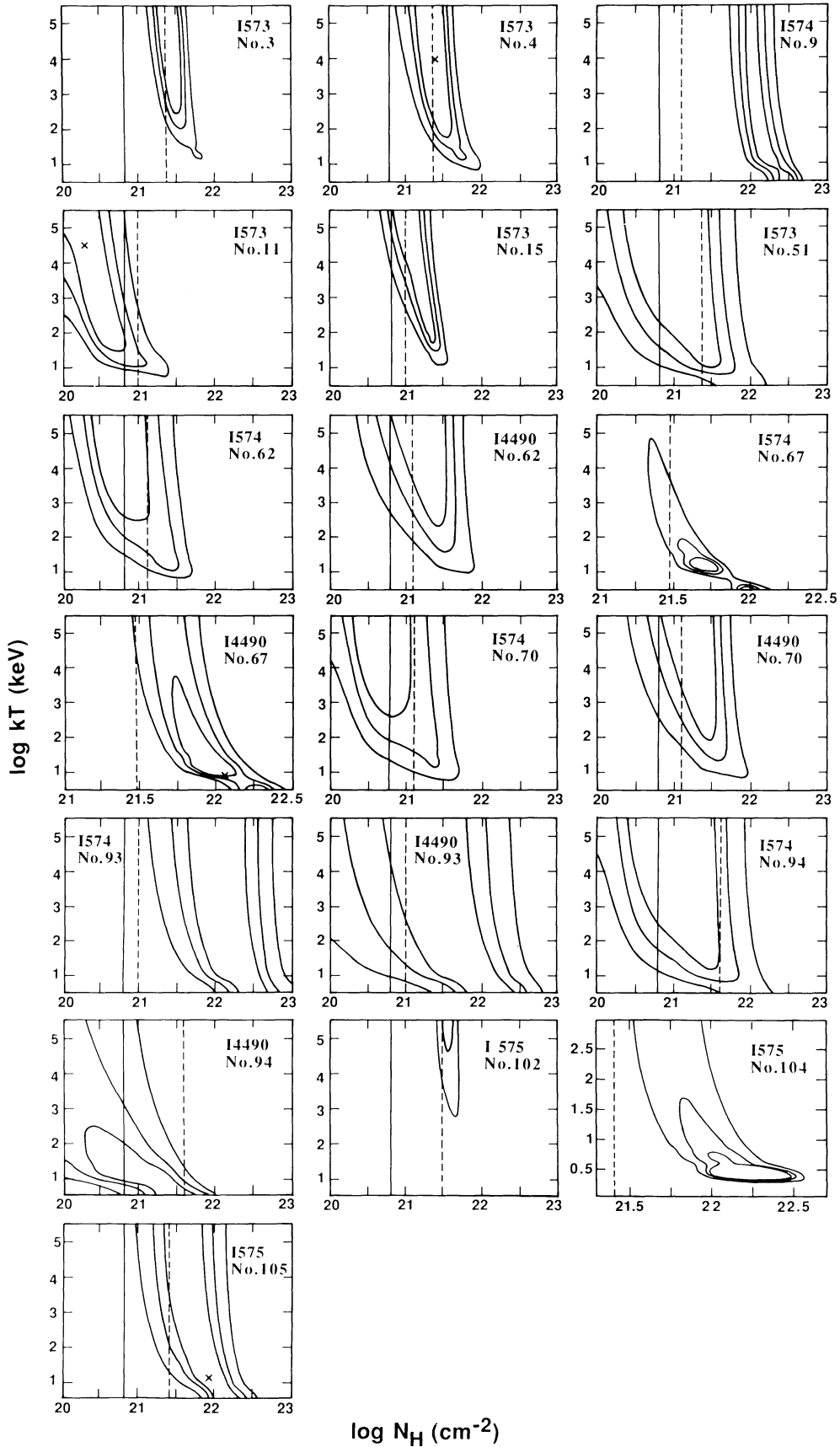
FIG. 7.—Confidence contours at 68%, 90%, and 99% from the spectral fits of bright X-ray sources in M31. The solid line indicates the galactic N_H; the dashed line, the N_H in M31 (see text).
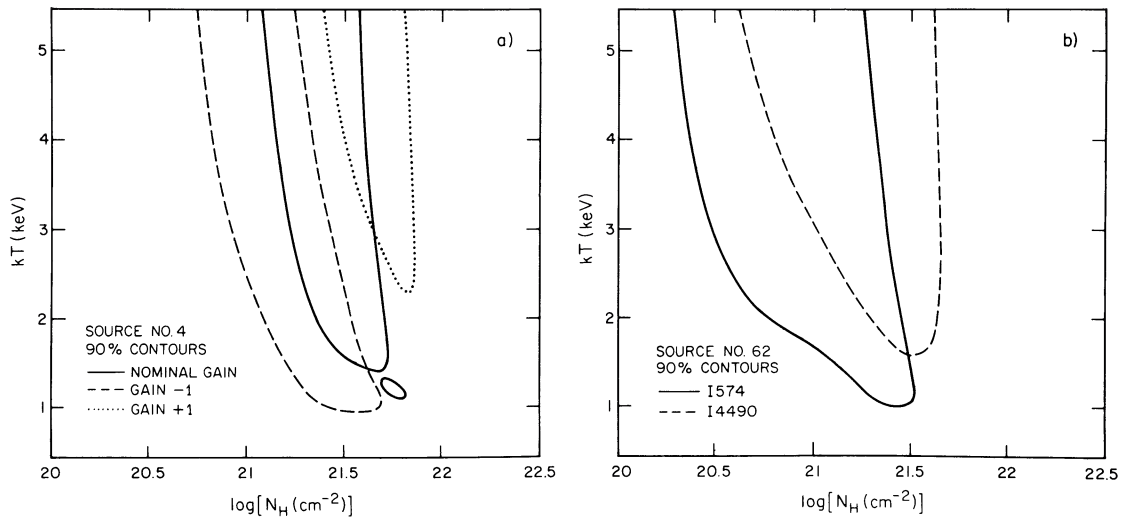
FIG. 8.—(a) Confidence contours at 90% for source 4 at nominal IPC gain and for extreme values of the gain; (b) 90% confidence contours for the two separate observations of source 62.
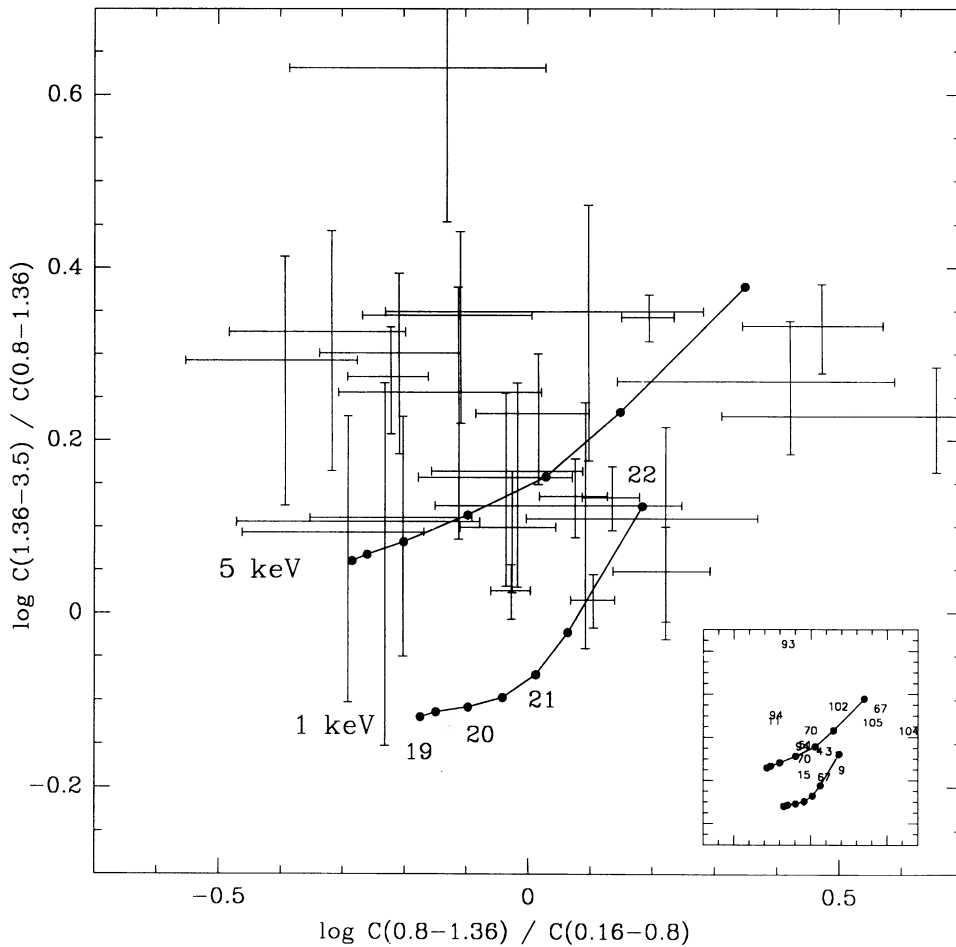
FIG. 9.—X-ray colors of the M31 sources. All detections with more than 100 counts in a single observation are included. The two curves show the loci of the two models of thermal emission with constant kT (1 and 5 keV) and varying N_H (10^{19}–10^{22} cm^{-2}). The insert show the X-ray colors of sources in Table 5.

same spectral model (Fabbiano et al. 1987). Of these four (sources 9, 104, and possibly 93 and 67) have N_H larger than that evaluated from the H I content of M31.

2.6.2. X-Ray Colors

Most IPC sources are detected with a smaller number of counts than the 14 sources discussed above, so that a χ^2 fit of the IPC spectral channels does not constrain the spectral parameters usefully. We attempted to obtain spectral information for all the sources detected in the IPC with 100 counts or more, by deriving X-ray colors, as described by Kim et al. (1991). These colors allow one to discriminate between temperature and absorption effects. They are defined as ratios between a soft (0.16–0.8 keV), an intermediate (0.8–1.36 keV) and a hard (1.36–3.5 keV) band within the *Einstein* energy range. Figure 9 shows the distribution of the X-ray colors of the M31 IPC sources detected with more than 100 counts. Colors for a bremsstrahlung model, with $kT = 1$ and 5 keV, and low-energy absorption ranging from $N_H = 10^{19}$ to 10^{22} are also plotted.

The results indicate that the bulk of the M31 sources are consistent with a spectrum of $kT > 1$ keV. About half of the sources do not require intrinsic absorption above the line of sight N_H. A few sources are soft and highly absorbed, in agreement with the results of the spectral fits. The distributions of colors of the M31 sources is similar to that found for spiral galaxies (Kim et al. 1991).

3. DISCUSSION

The *Einstein* observations of M31 have led to the detection of 108 sources (see Table 2), with luminosities ranging from $\sim 5 \times 10^{36}$ to over 10^{38} ergs s^{-1}. One source is positionally coincident with the companion galaxy M32, with a luminosity of 5×10^{37} ergs s^{-1}, and a few additional sources have been identified with foreground/background objects (Crampton et al. 1984). As discussed by Crampton et al. (1984), the identifications of the sources in M31 is not trivial, because of source confusion especially in the inner bulge region. In the outer parts, Crampton et al. were able to associate several sources with globular clusters, and some with blue stars in M31. Most sources do not have an optical or radio identification.

The total X-ray luminosity of M31 is $L_x \sim 3 \times 10^{39}$ ergs s^{-1} (for a thermal bremsstrahlung spectrum with $kT = 5$ keV, $N_H = 7 \times 10^{20}$ cm^{-2}, and for an average 10% vignetting correction). It is roughly equally divided between the bulge (i.e., $r < 5'$; Morton et al. 1977) and the disk region ($r > 5'$). The contribution from individual sources accounts for $\sim 75\%$ of the bulge luminosity, and for all of the disk emission. However, as noticed in § 2.4, we might be underestimating the contribution of large-scale diffuse emission in the disk.

3.1. Luminosity Distribution of Individual Sources in the Bulge and Disk of M31

The intrinsic luminosities of the X-ray sources in M31 are comparable to those of close accreting binary systems in our own Galaxy and in other nearby systems (cf. Peres et al. 1989—binary in M33) and suggest that most of them are indeed compact sources. Some of these sources are known to vary (see § 2.5; Collura et al. 1990), confirming their pointlike nature. Moreover, some of the identifications by Crampton et al. (1984) associate these bright X-ray sources with globular clusters and with blue stars, which also suggest both low-mass and massive close binaries.
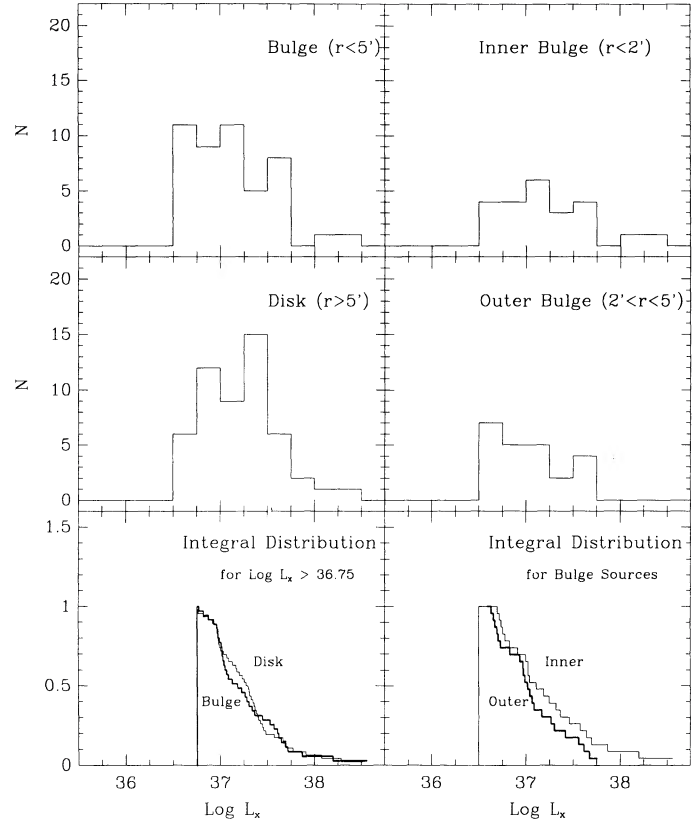
FIG. 10.—Luminosity distribution of sources within and outside a 5′ radius (*left*) and in the inner and outer bulge (*right*). The bottom two panels represent the comparison of the integral distributions of the disk and bulge sources with log $(L_x) > 36.75$ (*left*) and inner and outer bulge sources (*right*).

We show in Figure 10 the luminosity distribution of the sources in M31, plotted in four bins per decade. Sources inside and outside the bulge are shown in different panels and bulge sources at different radial distances from the galaxy's center are also shown. A plot of the individual source luminosity as a function of galactocentric distance is shown in Figure 11.

It is evident from both Figures 10 and 11 that there is no significant luminosity gradient for the X-ray sources in M31, and that the luminosity distribution of sources in the bulge and in the disk are not different. To quantify this statement, we have applied a Kolmogorov–Smirnov (K-S) test to the comparison of the cumulative distributions of inner-outer bulge sources, and bulge-disk sources (we have chosen a luminosity threshold of 36.75 for the bulge-disk comparison, to ensure a homogeneous sensitivity in the two regions). In both comparisons, we find a probability of $\sim 70\%$ of the two populations being drawn from the same parent population. This result is in contrast with earlier reports of Van Speybroeck et al. (1979) who suggested that the inner bulge contained a population with average X-ray luminosity higher than the outer bulge or the disk. This conclusion, however, was based on the analysis of only some of the data now available.

To estimate a functional description of the luminosity distribution of the bulge sources, a range of possible luminosity functions, in the form of power laws, have been compared to the luminosity distribution. We have chosen to use only the bulge sources, instead of using all the sources detected, to ensure that the X-ray data are as homogeneous as possible, i.e.,
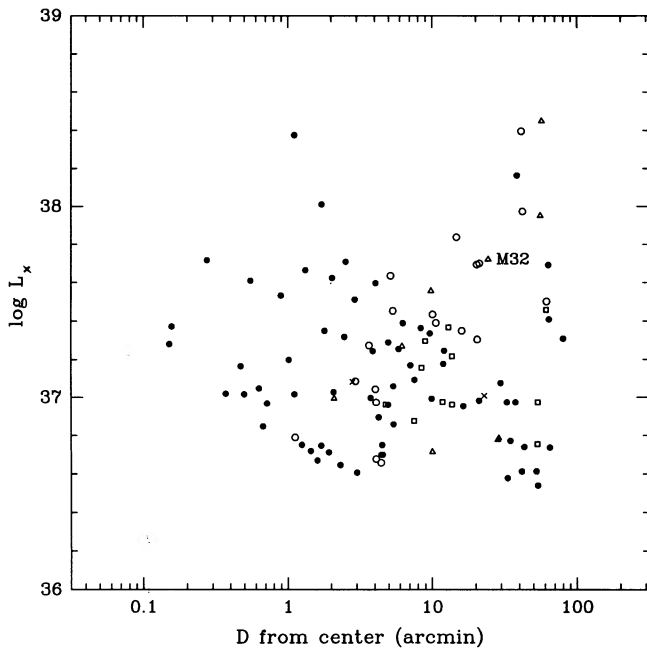
FIG. 11.—Luminosity distribution of the M31 sources at different radial distances from the center. Foreground and background sources are also included and plotted as if at the distance of M31. Identified sources (from Crampton et al. 1984) are plotted with different symbols as follows: *open circles*, G; *open squares*, B; *crosses*, G? or B?; *triangles*, background/foreground sources (luminosities calculated as if they were at the M31 distance); *dots*, unidentified objects.

that the fluxes are obtained from the same instrument at the same limiting sensitivity. Since the luminosity distributions of bulge and disk sources in M31 are consistent with each other (see above), the following results can be considered representative of M31 as a whole.

Figure 12 shows the luminosity distribution of the M31 sources within a 5′ radius from the center (taken at R.A. = 00^h40^m, decl. = $41°00'$; cf. Fig. 7). We can represent this distribution with a single power law, $N \propto L^\alpha$. To estimate the best-fit parameters and errors of this function, we have used the maximum likelihood method described in Crawford, Jauncey, & Murdoch (1970), and the results are shown in Figure 12. We have found that the best-fit slope, normalized to the data above $\log L_x = 36.75$, is $\alpha = -0.82$, and slopes between -1 and -0.66 are within the 68% confidence limits.

3.2. Diffuse Emission from the Bulge and Upper Limits to a Hot Gaseous Component

Although present studies do not agree on the explanation for the observed correlation between the X-ray and optical emission in early-type galaxies (see review by Fabbiano 1989, and references therein), there is a consensus that high-luminosity galaxies contain large quantities of hot gas (~ 0.1–0.01 of the luminous mass; Canizares Fabbiano, & Trinchieri 1987), and that radiation from this gas dominates the observed X-ray luminosity. It is likely that this property does not extend to lower luminosity objects, in which the contribution of individual sources may dominate. However, the optical mass/luminosity at which this transition occurs is still a matter of debate. Since many of the optical properties of spiral bulges

and of elliptical galaxies are very similar, the X-ray emission from the bulge of M31 has been used to estimate the "expected" X-ray properties of elliptical galaxies, and in particular to calibrate the point source contribution to the X-ray luminosity of early-type objects (Trinchieri & Fabbiano 1985). It is therefore important to set an observational limit on the amount of hot gas that could be present in the bulge of M31.

The individual sources detected in the bulge account for $\gtrsim 75\%$ of the total bulge luminosity. The residual emission, of $L_x \sim 6 \times 10^{38}$ ergs s^{-1} (for the spectral parameters of Table 2), is not resolved into individually detectable sources. In analogy with our own galaxy, we expect that sources of lower luminosity contribute to the emission, although they cannot be resolved individually with the present data.

To check this hypothesis, we have estimated the integrated luminosity that individual sources would produce, under the assumption that they are distributed according to the power-law functions derived above, extrapolated to lower luminosities with the same functional shape. In order not to exceed the total bulge luminosity, both functions at the 68% limits need to be either truncated or flattened at luminosities around $L_x \sim 10^{34}$ and 10^{35} ergs s^{-1}, for the flatter and steeper function, respectively. This is well within the range of luminosities for discrete Galactic X-ray sources (see Watson 1990).

This result indicates that individual X-ray sources could explain all of the emission from the bulge of M31 in the *Einstein* energy band and that there is no requirement for other significant components of the X-ray emission.

Nevertheless, we can use the "diffuse" bulge emission to estimate an upper limit to the amount of a hot gaseous component. The most conservative assumption that we can make is that *all* of the residual emission not accounted for by the individual sources is to be attributed to this component. If we assume a gas with a temperature kT around 1 keV, typical of
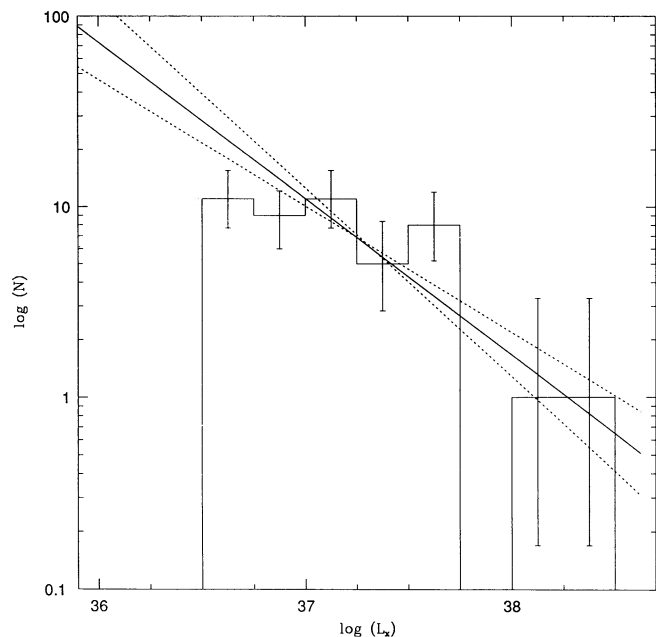
FIG. 12.—Luminosity distribution of bulge sources ($r < 5'$). The best-fit power law $N = A \times L_x^{-0.8}$ (*solid line*), and the 68% confidence error lines (*dotted*) are also shown.

early-type galaxies (Trinchieri et al. 1986; Forman, Jones, & Tucker 1985). and we attribute all photons not in individual sources to this gaseous component (see § 2.4), we obtain $L_x(gas) \sim 4 \times 10^{38}$ ergs s^{-1}. This would indicate that the gas has a mass $M_{gas} \sim 2 \times 10^6 \ M_\odot$, if the gas fills uniformly the bulge region (i.e., within a radius $r \sim 5'$). This is therefore also a firm upper limit on the amount of hot gas in the bulge, since any amount of clumpiness would reduce these estimates.

It is very unlikely that single sources abruptly stop below the observational sensitivity limit. Therefore, $2 \times 10^6 \ M_\odot$ can be regarded as a very conservative upper limit to the hot gas content of the bulge. This limit is comparable to those derived from the optical H I and *IRAS* data (see Ciardullo et al. 1987).

The expected input from stellar mass loss in the bulge is of the order of $\dot{M} \sim 0.05 \ M_\odot$ yr^{-1} (Jacoby 1980). If the rate has been constant over the galaxy's lifetime at this value, the total amount of gas produced would be $\sim 8 \times 10^9 \ M_\odot$. Since there is little evidence that the gas is recycled into producing stars (estimates from *IUE* data indicate a star formation rate of $\sim 7.4 \times 10^{-5} \ M_\odot$ yr^{-1}; Deharveng et al. 1982), most of the gas must have been lost from the system.

3.3. *Nature and Formation of Bulge Sources*

The sources found within $r \sim 5'$ from the center most likely are in the bulge, with the exception of source 45, identified with a globular cluster (Crampton et al. 1984). Although an individual study of their spectral parameters is not possible, their integrated spectrum is consistent with a population of "soft" X-ray binaries with no intrinsic absorption (Fabbiano et al. 1987; Makishima et al. 1989). Their high luminosity, the stellar population of the bulge, and the typical X-ray temperatures moreover would be indicative of low-mass binaries.

These sources seem to be spatially aligned in a "barlike" east-west distribution, as noted in the early papers on the *Einstein* observations of M31 (Van Speybroeck et al. 1979; Van Speybroeck & Bechtold 1981; Long & Van Speybroeck 1983), and they appear to be strongly concentrated in the inner bulge region. The coincidence of this enhanced source distribution with a reported hole in the distribution of optical novae led Vader et al. (1982) to suggest that these sources could be the result of the evolution of a dead cataclysmic variable population that had long since undergone its nova phase. More recent observations, however, have dispelled the notion of a nova hole in M31 (Ciardullo et al. 1987) and have led to the

suggestion that the bulge sources of M31 may be the remnants of disrupted globular clusters (similar to those suggested by Grindlay 1984 for the Milky Way bulge sources).

To explore further these issues we have compared the distribution of the bulge sources of M31 with that of the optical novae (from Ciardullo et al. 1987), and with that of the tilted disk of ionized gas found recently in the inner bulge of M31 (Jacoby, Ford, & Ciardullo 1985; Ciardullo et al. 1988), which also suggests an east-west symmetry. When we compare the radial isophotal distributions of novae and X-ray sources with a Kolmogorov-Smirnov test, they are consistent. However, the azimuthal distributions are different.

Figure 13 shows the positions of the bulge sources plotted in the same scale and reference frame as those of the novae. Comparison of the two plots clearly shows that the azimuthal distributions are different. Quantitatively, this is confirmed by a 2×2 contingency table test, based on the comparison of the number of X-ray sources and novae in 90° quadrants centered on the optical axes of the bulge, which gives a $\chi^2_{1DOF} = 7.1$ ($P \sim 7 \times 10^{-3}$ that X-ray sources and novae both belong to the same population).

Figure 14 (Plate 8) shows the HRI contour map of the bulge of M31 overlaid onto the Hα image of the bulge of Ciardullo et al. (1988). In contrast to the previous result, this comparison suggests a puzzling resemblance between the distribution of X-ray sources and that of the Hα emission.

These results are somewhat confusing. The stringent limits on star formation posed by the UV observations of the bulge of M31 (Deharveng et al. 1982) make it unlikely that the apparent connection between the X-ray source distribution and the Hα emission is due to the presence of X-ray sources belonging to a young stellar population. A significant population of massive binaries is also excluded by the X-ray spectrum of the bulge (see above). It is also unlikely that these X-ray sources belong to a separate subsystem, such as a bar, because there is no evidence of a bar in the stellar light and in the distribution of optical novae. The latter is particularly relevant because optical novae and X-ray-luminous low-mass binaries (such as those that we detect in M31) are thought to be smaller systems, both low-mass binaries with different mass primary objects (white dwarf and neutron star, respectively). Since the total mass of the binary system is likely to be similar in the two cases, postulating the existence of a separate dynamical system for the X-ray sources is unwarranted.
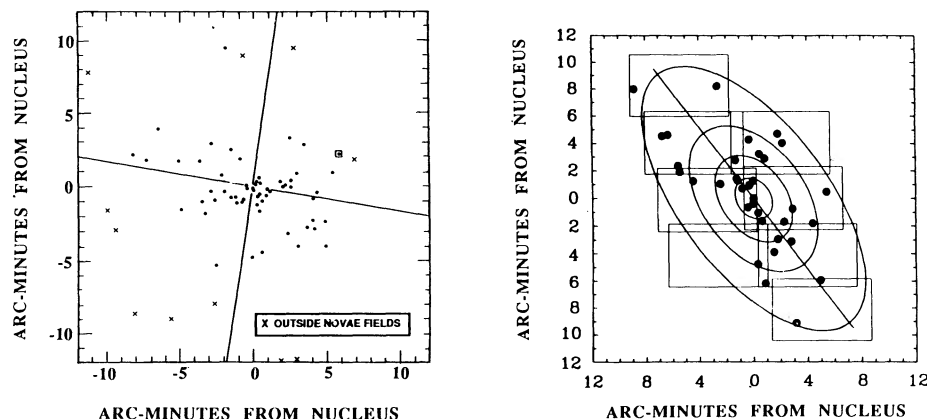
FIG. 13.—Comparison of the spatial distributions of the optical novae (from Ciardullo et al. 1987) (*right*) and of the X-ray sources within $12' \times 12'$ from the galaxy's center (*left*).

PLATE 8
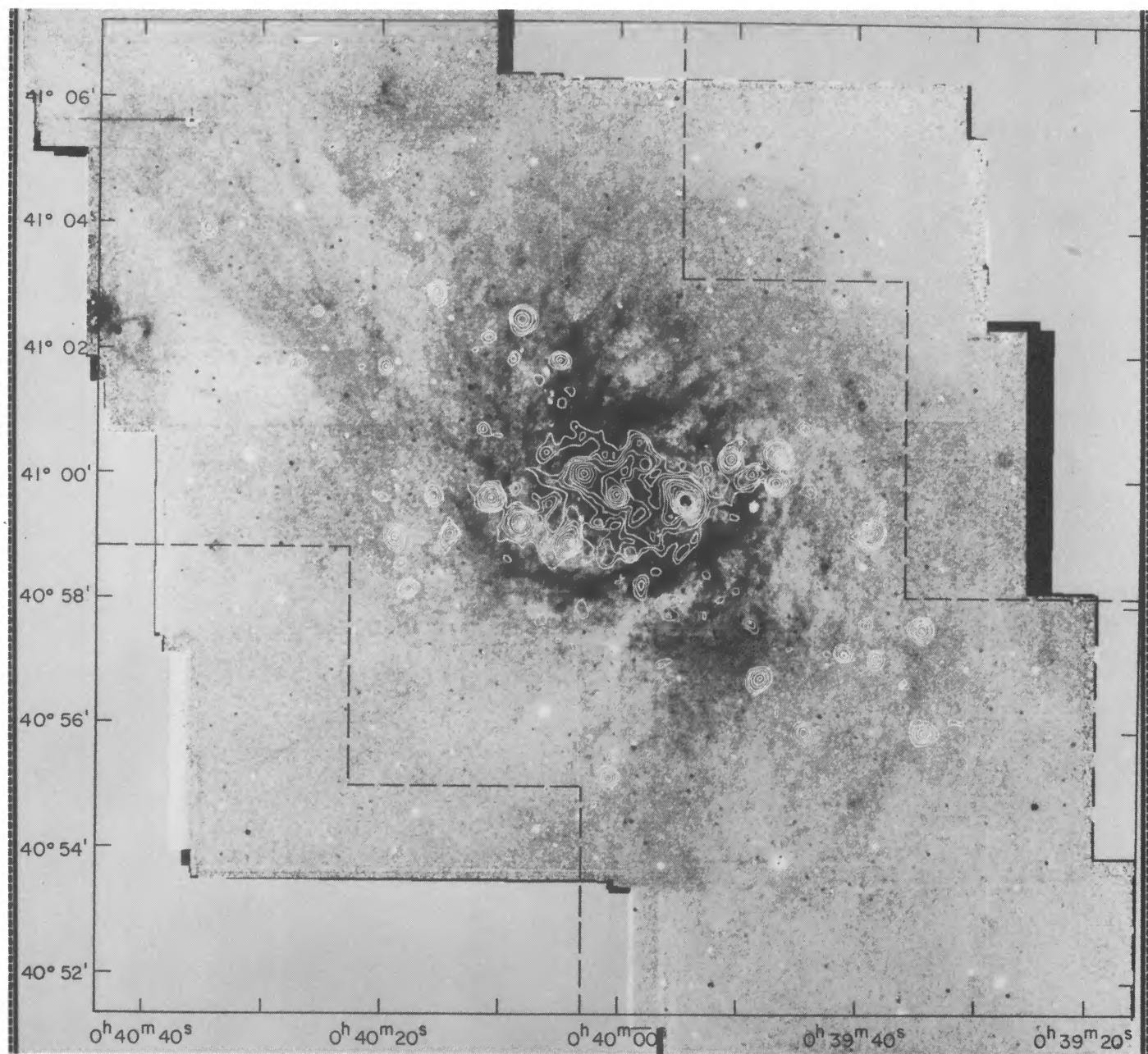
FIG. 14.—Comparison of the X-ray source distribution and of the Hα emission in the bulge of M31. The Hα map is from Ciardullo et al. (1988). The X-ray data from the HRI are at a resolution of 4″ pixel⁻¹ and have been smoothed with a Gaussian with $\sigma = 8''$.

TRINCHIERI & FABBIANO (see 381, 97)

If the X-ray sources do not belong to a separate dynamical system from the overall bulge, nor to a different stellar population, then one might postulate that the dynamical subsystem identified by the gaseous inner disk plays a role in the formation or existence of low-mass X-ray binaries, which would also determine the geometry of the spatial distribution of the X-ray sources. Then one should look for ways in which the impact of a low-mass binary with the gaseous inner disk may trigger accretion onto the neutron star resulting in X-ray emission.

Exploring such models is beyond the scope of the present paper. However, we note that the geometry of the distribution of X-ray sources puts constraints on models of low-mass X-ray binaries. In particular, models for low-mass X-ray binaries with lifetimes of the order of 10^{8-9} yr (e.g., van den Heuvel 1983) are at odds with this distribution, because typical orbital times for bulge sources in M31 are $\sim$ a few $\times 10^7$ yr. Therefore, even if sources were turned on in a east-west alignment, they would have had ample time to disperse throughout the bulge. However, a recent model for the evolution of low-mass X-ray binaries suggests that, under suitable conditions, lifetimes could be $\leq 10^7$ yr (Ruderman, Shaham, & Tavani 1989), more in agreement with the M31 data.

3.4. Spectral Properties and the Identification of X-Ray Sources

As discussed in § 2.6, eight of the bright sources in the outer regions of M31 have cutoffs that suggest N_H in excess of the Galactic line-of-sight absorption column. Figure 15 displays a comparison between the X-ray–derived N_H and the N_H derived from the H I observations of M31 (see Table 5), and from the reddening applied to the $(B-V)$ of the optical counterparts by Crampton et al. (1985). The identifications of Crampton et al. (1984) are also listed in Figure 15. As can be seen from this figure, sources 9, 93, 104, and perhaps 67 have an X-ray–absorbing column larger than the H I or optical N_H. For the other sources the X-ray and the H I N_H are in agreement, suggesting that no intrinsic absorption to the X-ray source is required and that they may just be on the far side of the disk of M31.

Of the eight sources displayed in Figure 15, five are identified with globular clusters (sources 4, 9, 67, 102, and 105). One or

two of these (9, and possibly 67) have intrinsic X-ray absorption uncharacteristic of low-mass binaries (e.g., see Fabbiano, et al. 1987). Moreover, source 67 has a very low value of kT (see § 2.6), below the "normal" range of those in binary X-ray sources. Source 104, for which there is no optical identification, has a similar X-ray spectrum. These spectral parameters suggest that sources 9 and 67 might have been misidentified, unless they represent a new class of globular cluster sources. It should be noted in fact that the positional coincidence of these sources with the proposed optical counterparts is remarkable, and that the probability of a chance association is very low (see Crampton et al. 1984). For the other three globular clusters, comparison with the optical reddening supports the identification of sources 102 and 4. However, there is no comparable optical reddening in source 105, suggesting that perhaps the identification with the globular cluster is wrong.

4. SUMMARY AND CONCLUSIONS

One hundred eight individual sources have been detected in M31, with X-ray luminosities in the range $L_x \sim 5 \times 10^{36}$ to $> 10^{38}$ ergs s^{-1}. About one-half of them are located within the bulge, and several have been identified with globular clusters or blue stellar systems in the disk (Crampton et al. 1984). No significant difference is found between the luminosity distribution of sources inside and outside the bulge, nor within the bulge itself.

The total X-ray emission from M31, $L_x \sim 3 \times 10^{39}$ ergs s^{-1}, can be accounted for by emission from individual sources. However, our background subtraction method would lead to underestimating any large-scale diffuse emission from the disk. We have estimated a conservative upper limit to the amount of hot gas that can be present in the bulge, of $M_{gas} < 2 \times 10^6$ $M_\odot$. This is comparable to the limits of colder gas estimated from the IRAS and H I data (Ciardullo et al. 1987), suggesting that most of the gas produced in the stellar evolution is lost from the system.

The spatial distribution of the X-ray bulge sources is at odds with the distribution of the old stellar population, from which they should originate. The similarity with the morphology of the disk of ionized gas in the inner bulge region might suggest a link between the formation of low-mass binaries and the presence of the gaseous disk. Moreover, since it is unlikely that the X-ray sources are in a separate dynamical subsystem within the bulge, their distribution poses constraints to their evolution time scales. To retain their distinct geometry, their lifetime should be shorter than the dynamical time scale of the stars in the bulge, of a few $\times 10^7$ years.

The spectral results on some of the brightest sources indicates a large low-energy cutoff, larger than the Galactic line-of-sight value. Most of them are identified with globular clusters. This suggests that either some of the identifications are wrong, or that the brightest X-ray sources are systematically located behind the H I ring in M31. Their luminosities, corrected for the effects of absorption, could increase by a factor of 2 or more. This would widen even more the discrepancy between the luminosity distribution of the globular cluster sources in M31 and in our own galaxy (cf. Long & Van Speybroeck 1983). A better measure of the X-ray spectral parameters, which will be possible with the AXAF instruments, will be able to identify these as globular cluster sources or massive binaries in the disk; furthermore better X-ray positions, achievable with the higher spatial resolution of AXAF, will provide more secure
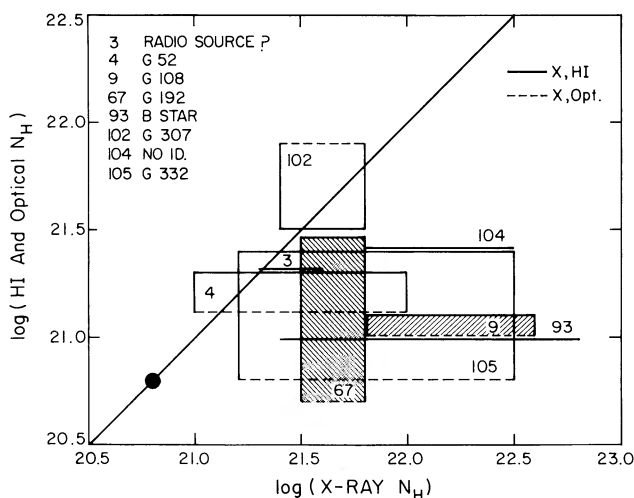
FIG. 15.—Comparison of H I and optical absorbing columns with the X-ray N_H. The diagonal line is the locus of equal "X-ray" N_H and H I/optical N_H. The dot represents the line of sight Galactic column density to M31.

identifications with objects in M31, and more examples that are needed to further address these issues.

We have benefited from many useful discussions with J. Gallagher, S. Kent, J. McClintock, M. Elvis, F. Primini, & L. Van Speybroeck. S. Kent has provided us with the optical radial

profile of the bulge of M31. D.-W. Kim has provided software for the derivation of X-ray colors. S. Hazelton and L. Kim have assisted in the data analysis. We thank J. Halpern for pointing out the identification of sources 11 and 15 with external active galaxies. This work was partially supported by the NASA contract NAS8-30751 and by the Italian ASI.

REFERENCES

Baade, W., & Swope, H. H. 1963, AJ, 68, 435
Blair, W. P., Kirshner, R. P., & Chevalier, R. A. 1981, ApJ, 247, 879
Canizares, C. R., Fabbiano, G., & Trinchieri, G. 1987, ApJ, 312, 503
Capaccioli, M., Della Valle, M., D'Onofrio, M., & Rosino, L. 1989, AJ, 97, 1622
Ciardullo, R., Ford, H. C., Jacoby, G. H., & Shafter, A. W. 1987, ApJ, 318, 520
Ciardullo, R., Ford, H. C., Shafter, A. W., Neill, J. D., & Jacoby, G. H. 1988, AJ, 95, 438
Collura, A., Reale, F., & Peres, G. 1990, ApJ, 356, 119
Crampton, D., Cowley, A. P., Hutchings, J. B., Shade, D. J., & Van Speybroeck, L. 1984, ApJ, 284, 663
Crampton, D., Cowley, A. P., Shade, D., & Chayer, P. 1985, ApJ, 288, 494
Crawford, D. F., Jauncey, D. J., & Murdoch, H. S. 1970, ApJ, 162, 405
Deharveng, J. M., Joubert, M., Monnet, G., & Donas, J. 1982, A&A, 106, 16
Emerson, D. T. 1974, MNRAS, 169, 607
Fabbiano, G. 1989, ARA&A, 27, 87
Fabbiano, G., Trinchieri, G., & Van Speybroeck, L. 1987, ApJ, 316, 127
Forman, W., Jones, C., & Tucker, W. 1985, ApJ, 293, 102
Giacconi, R., et al. 1979, ApJ, 230, 540
Grandi, S. A., & Osterbrock, D. E. 1978, ApJ, 220, 783
Grindlay, J. E. 1984, Adv. Space Res., 3, 19
Halpern, J. P., & Oke, J. B. 1987, ApJ, 312, 91
Harnden, F. R., Fabricant, D. G., Morris, D. E., & Schwarz, J. 1984, Scientific Specification of the Data Analysis System for the Einstein Observatory (HEAO 2) IPC (Internal SAO Special Report 393)
Jacoby, G. H. 1980, ApJS, 38, 351
Jacoby, G. H., Ford, H., & Ciardullo, R. 1985, ApJ, 290, 136
Kim, D.-W., Fabbiano, G., & Trinchieri, G. 1991, in preparation
Long, K. S., & Van Speybroeck, L. 1983, in Accretion Driven X-Ray Sources, ed. W. Lewin & E. P. J. van den Heuvel (Cambridge: Cambridge Univ. Press), 41

Maccacaro, T., Garilli, B., & Mereghetti, S. 1987, AJ, 93, 1484
Makishima, K., et al. 1989, PASP, 41, 697
Mauche, C. W., & Gorenstein, P. 1986, ApJ, 302, 371
Morton, D. C., Andereck, C. D., & Bernard, D. A. 1977, ApJ, 212, 13
Peres, G., Reale, F., Collura, A., & Fabbiano, G. 1989, ApJ, 336, 140
Ruderman, M., Shaham, J., & Tavani, M. 1989, ApJ, 336, 507
Stark, A. A., et al. 1991, ApJ, submitted
Trinchieri, G., & Fabbiano, G. 1985, ApJ, 296, 447
Trinchieri, G., Fabbiano, G., & Canizares, C. R. 1986, ApJ, 310, 127
Trinchieri, G., Fabbiano, G., & Romaine, S. 1990, ApJ, 356, 110
Vader, J. P., van den Heuvel, E. P. J., Lewin, W. H. G., & Takens, R. J. 1982, A&A, 113, 328
Unwin, S. C. 1980a, MNRAS, 190, 243
———. 1980b, MNRAS, 190, 551
van den Heuvel, E. P. J. 1983, in Accretion Driven X-Ray Sources, ed. W. Lewin & E. P. J. van den Heuvel (Cambridge: Cambridge Univ. Press), 303
Van Speybroeck, L. S., & Bechtold, J. 1981, in X-Ray Astronomy with the Einstein Satellite, ed. R. Giacconi (Dordrecht: Reidel), 153
Van Speybroeck, L., Epstein, A., Forman, W., Giacconi, R., Jones, C., Liller, W., & Smarr, L. 1979, ApJ, 234, L45
Watson, M. 1990, in Windows on Galaxies, ed. G. Fabbiano, J. S. Gallagher, & A. Renzini, (Dordrecht: Kluwer) 177
Zwicky, F., Oke, J. B., Neugebauer, G., Sargent, W. L. W., & Fairall, A. P. 1970, PASP, 82, 93